nature communications

Article

https://doi.org/10.1038/s41467-025-58074-0

Smoking aggravates neovascular age-related macular degeneration via Sema4D-PlexinB1 axis-mediated activation of pericytes

Received: 18 January 2024

Accepted: 4 March 2025

Kai He[1,9], Xue Dong[1,2,9], Tianjing Yang[3,9], Ziqi Li[1], Yuming Liu[1], Jing He[4], Meng Wu[1,2], Selena Wei-Zhang[1], Parhat Kaysar[1], Bohao Cui[1], Xueming Yao[3], Li Zhang[5], Wei Zhou[1], Heping Xu[6], Jun Wei[7], Qiang Liu[8], Junhao Hu[4] ✉, Xiaohong Wang[1,2] ✉ & Hua Yan[1,3] ✉

Age-related macular degeneration (AMD) is a prevalent neuroinflammation condition and the leading cause of irreversible blindness among the elderly population. Smoking significantly increases AMD risk, yet the mechanisms remain unclear. Here, we investigate the role of Sema4D-PlexinB1 axis in the progression of AMD, in which Sema4D-PlexinB1 is highly activated by smoking. Using patient-derived samples and mouse models, we discover that smoking increases the presence of Sema4D on the surface of $CD8^+$ T cells that migrate into the choroidal neovascularization (CNV) lesion via CXCL12-CXCR4 axis and interact with its receptor PlexinB1 on choroidal pericytes. This leads to ROR2-mediated PlexinB1 phosphorylation and pericyte activation, thereby disrupting vascular homeostasis and promoting neovascularization. Inhibition of Sema4D reduces CNV and improves the benefit of anti-VEGF treatment. In conclusion, this study unveils the molecular mechanisms through which smoking exacerbates AMD pathology, and presents a potential therapeutic strategy by targeting Sema4D to augment current AMD treatments.

Age-related macular degeneration (AMD) is a neuroinflammatory disease and is recognized as the predominant cause of irreversible vision loss among the elderly population globally[1], with its prevalence on the rise due to an aging population[1,2]. The most prominent risk factors of AMD are increasing age and cigarette smoking[3]. A substantial number of research from various study types, including case-control, population-based, and prospective studies, consistently establishes cigarette smoking as the preeminent and widely recognized modifiable risk factor for AMD. It imparts an acceleration of disease onset by approximately a decade[3]. Moreover, the correlation between smoking and AMD exhibits a conspicuously dose-dependent correlation, with a direct association between daily cigarette consumption and a

---

[1]Department of Ophthalmology, Laboratory of Molecular Ophthalmology and Tianjin Key Laboratory of Ocular Trauma, Ministry of Education International Joint Laboratory of Ocular Diseases, Tianjin Institute of Eye Health and Eye Diseases, China-UK “Belt and Road” Ophthalmology Joint Laboratory, State Key Laboratory of Experimental Hematology, Tianjin Medical University General Hospital, Tianjin, China. [2]Department of Pharmacology, Tianjin Key Laboratory of Inflammation Biology, The Province and Ministry Co-sponsored Collaborative Innovation Center for Medical Epigenetics, School of Basic Medical Sciences; Tianjin Medical University, Tianjin, China. [3]School of Medicine, Nankai University, Tianjin, China. [4]Laboratory of Vascular Biology and Organ Homeostasis, Interdisciplinary Research Center on Biology and Chemistry, Shanghai Institute of Organic Chemistry, Chinese Academy of Sciences, Shanghai, China. [5]Department of Ophthalmology, The Second Affiliated Hospital of Chongqing Medical University, Chongqing, China. [6]The Wellcome-Wolfson Institute for Experimental Medicine, Queen’s University Belfast, Belfast, UK. [7]Institute of Hematology & Blood Diseases Hospital, Chinese Academy of Medical Sciences & Peking Union Medical College, Tianjin, China. [8]Department of Neurology, Tianjin Neurological Institute, Tianjin Institute of Immunology, Tianjin Medical University General Hospital, Tianjin, China. [9]These authors contributed equally: Kai He, Xue Dong, Tianjing Yang. ✉e-mail: jhhu@sioc.ac.cn; xiaohongwang@tmu.edu.cn; zyyyanhua@tmu.edu.cn

heightened propensity to manifest choroidal neovascularization (CNV) and geographic atrophy[4].

AMD clinically manifests in two predominant forms: non-neovascular and neovascular. The latter, known as neovascular AMD (nvAMD), is characterized by CNV, where abnormal blood vessels sprout into the subretinal space and neuroretina. This abnormal vessel growth leads to blood vessel leakage, edema, and hemorrhage, culminating in precipitous central vision decline when left untreated. The introduction of anti-vascular endothelial growth factor (VEGF) therapy in 2006 marked a pivotal advance in AMD management, offering an efficacious approach to mitigate disease progression and restore visual function. However, the effectiveness of anti-VEGF therapy remains limited. Only a subset, ~30–35% of nvAMD patients, experience significant improvement in vision[5], while a substantial cohort of patients not achieving a complete response to this therapeutic regimen. Cigarette smoking has been linked to a two- to four-fold rise in the occurrence of nvAMD[6], along with a diminished effectiveness of anti-VEGF treatment[7]. Despite oxidative damage to the retina caused by smoking have been implicated, the specific mechanism through which smoking impacts the retina remains largely unclear.

Pericytes and endothelial cells (ECs) are fundamental components that constitute blood vessels. The function of blood vessels is not solely regulated by ECs but is also influenced by pericytes. Pericytes are defined as mural cells that envelop the endothelium of microvessels. They are embedded within the same basement membrane as ECs and interact closely with them. In contrast, the other mural cell type, vascular smooth muscle cells (vSMCs), covering large arteries and veins, are physically separated from the ECs by an intimal layer of extracellular matrix (ECM)[8]. Pericytes play a pivotal role in the formation and maintenance of the vasculature, and their dysfunction contributes to vascular-related disorders. In cases where pericyte coverage is reduced, or interactions between ECs and pericytes are compromised, blood vessels become unstable and exhibit increased leakage in various pathological conditions[9,10]. Pericytes have also been revealed to have significant implications in the context of cancer, lung injury, and fibrosis[11]. Studies have shown that pericytes can shield ECs from anti-angiogenic drugs, such as bevacizumab, particularly in tumor settings. Combination treatment with a PDGFRβ tyrosine kinase inhibitor (eliminating PDGFRβ positive pericytes) along with VEGF inhibition has proven to be more effective in blocking tumor angiogenesis than anti-VEGF therapy alone in various animal models[12]. In the context of CNV, it is established that pericytes also cover the newly formed capillaries, playing a crucial role in the growth and stability of the choroidal vessel network[6]. However, the precise contributions of pericytes to angiogenesis and anti-angiogenic therapy in CNV, along with their regulatory mechanisms, remain enigmatic.

The semaphorin-plexin system serves as a versatile intercellular signaling network, playing crucial roles during both development and in the mature organism. These interactions are pivotal for cell-to-cell communication processes that regulate cell migration, proliferation, and differentiation across various systems, including the nervous, immune, and skeletal systems. Moreover, the semaphorin-plexin signaling has demonstrated its importance in various vascular pathophysiological processes[13,14]. Sema4D is a semaphorin that exists in both transmembrane and secreted forms, and it interacts with its high-affinity receptor, PlexinB1[15].

In this study, we unveil a previously undiscovered function of the Sema4D-PlexinB1 signaling pathway as a critical regulator of CNV, a condition potentially induced by smoking. Specifically, $CD8^+$ T cells express Sema4D in response to smoking, initiating signals to PlexinB1 on pericytes, thereby activating pericytes and promoting the progression of CNV. We comprehensively investigated the role of the Sema4D-PlexinB1 signaling pathway in CNV and delved into the underlying mechanisms using samples from AMD patients and relevant mouse models.

Results

Cigarette smoking reduces anti-VEGF therapy efficacy in nvAMD patients

First, we aimed to explore whether cigarette smoking affects the responsiveness to anti-angiogenic therapy in nvAMD patients. 97 AMD patients were divided into two groups: active smokers (50 individuals, including 27 males and 23 females) and non-smokers (47 individuals, including 27 males and 20 females) (Supplementary Table 1). All patients received standard 3 + *pro re nata* (PRN; as needed) anti-VEGF therapy. Retinal thickness and the thickness of the damaged area in nvAMD were measured using optical coherence tomography (OCT) before treatment and after each treatment (Fig. 1A). While there were no differences in retinal and lesion thickness between the two groups before treatment (Fig. 1B, C), after three treatments, both retinal thickness and lesion thickness were significantly higher in the active smokers' group compared to the non-smokers' group (Fig. 1D, E). This suggests that cigarette smoking reduced the responsiveness to anti-VEGF therapy. Furthermore, only the age-onset of nvAMD in the active smokers' group was significantly lower than that in the non-smoking group (Fig. 1F, Supplementary Table 1), while the probability of complications, including macular edema, retinal detachment, ellipsoid zone reflectivity, and pigment epithelial detachment were increased in the active smokers' group (Supplementary Fig. 1A).

Cigarette smoking aggravates laser-induced CNV in mice

Next, we tested the effect of cigarette smoking on CNV in mice. We exposed one group of mice to a smoke exposure system for two months, while another group of mice received filtered air for the same duration, serving as the control. During the exposure period, the smoke-exposed mice failed to gain weight compared with the air-exposed mice (Supplementary Fig. 1B). However, there were no significant changes in the function and structure of the eyes, as evaluated by OCT and electroretinography (ERG) (Supplementary Fig. 1C–M). After two months of exposure, we employed a laser-induced photocoagulation model of CNV (laser-induced CNV model), in which laser burns of Bruch's membrane trigger vessel growth from the choroid[16]. Fundus fluorescein angiography (FFA) results showed that smoke exposure significantly increased vascular leakage on day 7 after laser photocoagulation (Fig. 1G, H). CD31 staining of the whole-mount retinal pigment epithelium (RPE)-choroid complex also demonstrated that smoke exposure increased the CNV volume (Fig. 1G, I), suggesting that it promoted choroidal neovessels formation.

Elevated Sema4D expression in retina-choroid complex of smoke-exposed mice

To investigate the underlying mechanism of smoking-aggravated CNV, we conducted transcriptome analysis of the retina-choroid complex from mice exposed to smoke or air, both with and without laser coagulation (smoke group, Ctrl group, smoke + CNV group, and CNV group, respectively). To identify the gene expression signature associated with smoking, we first compared the smoke group to the Ctrl group (mice without laser coagulation). A total of 1811 genes were significantly altered (1237 upregulated and 574 downregulated genes). Interestingly, gene ontology (GO) analysis revealed that semaphorin receptor activity was one of the most significantly enriched biological processes among the upregulated genes in the smoke group (Fig. 1J). Gene set enrichment analysis (GSEA) further confirmed the significant enrichment of the Sema/Plexin signaling pathway in the smoke group (Fig. 1K). To identify the specific semaphorins, we screened the expression of semaphorins in smoke-exposed and air-exposed mice, both with and without laser coagulation, using RNA-seq data. While multiple semaphorins were increased by CNV, Sema4D was the only semaphorin that was increased in response to smoke exposure in both control mice and CNV mice (Fig. 1L).

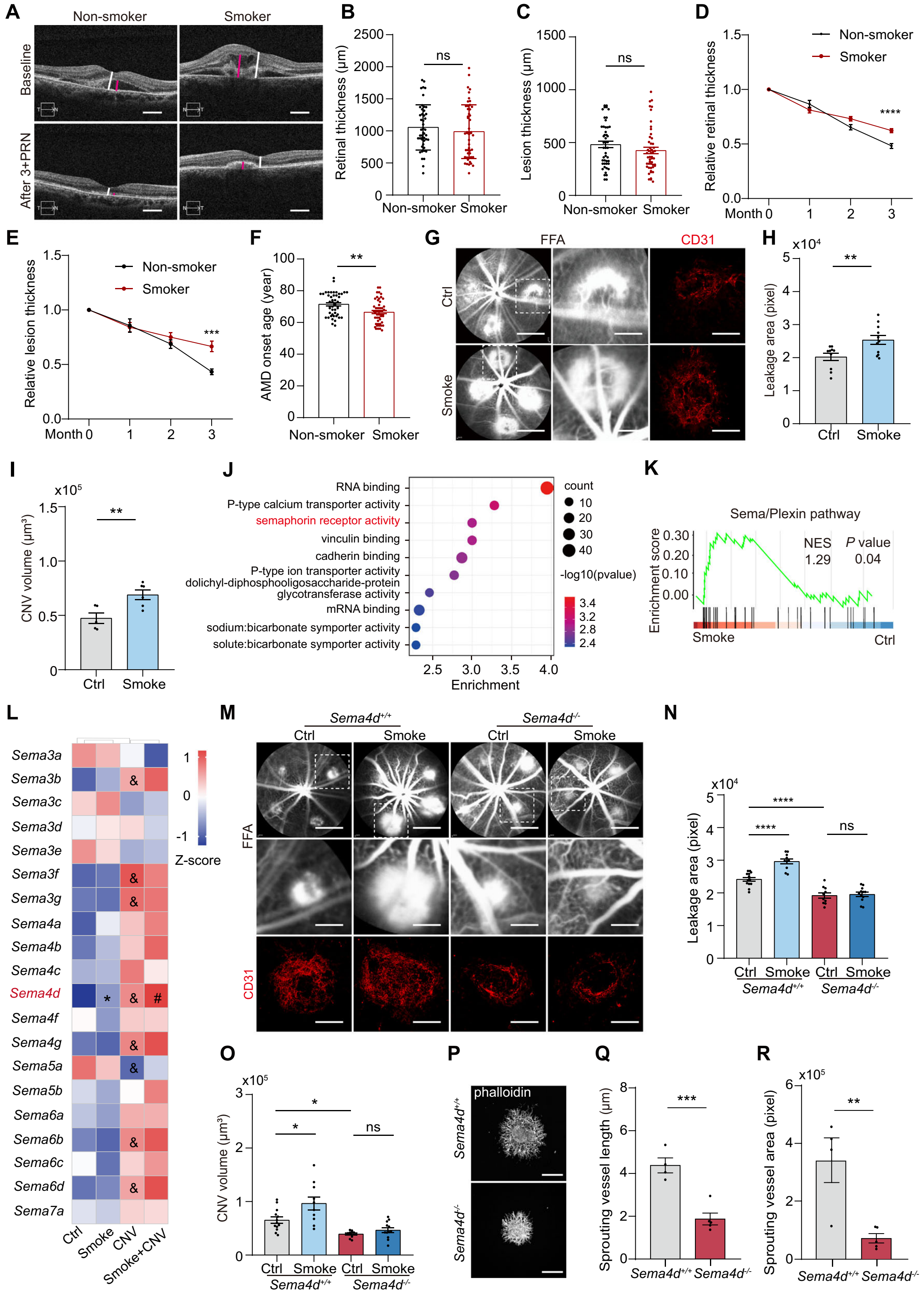

The elevated expression of Sema4D in the retina-choroid complex of smoke-exposed mice prompted us to analyze its function in the CNV model using *Sema4d*$^{-/-}$ mice. Vascular leakage area quantification and CD31 staining of the whole-mount RPE-choroid complex revealed that *Sema4d* knockout significantly alleviated vascular leakage and reduced CNV volume (Fig. 1M–O). Interestingly, while smoking increased the vascular leakage area and CNV volume in *Sema4d*$^{+/+}$ mice, the effect was diminished in *Sema4d*$^{-/-}$ mice (Fig. 1M–O), suggesting that Sema4D is essential in mediating smoking-aggravated CNV in mice. We also employed an ex vivo-choroid explant model for studying choroidal sprouting angiogenesis after CNV, which we had previously established[17]. Explants from *Sema4d*$^{-/-}$ mice displayed significantly reduced sprouting length and sprouting area (Fig. 1P–R). Conversely, when we treated CNV choroidal explants with either a vehicle or

Fig. 1 | Impact of Smoking on Anti-VEGF Treatment in nvAMD and CNV in Mice. **A** OCT images show baseline and post-treatment retinas in non-smokers and smokers with nvAMD. **B**, **C** Baseline retinal (B), lesion (C) thickness in nvAMD patients ($n = 47/50$). Mean ± SEM, $P = 0.2949$, 0.4062 (two-tailed Student's t test). **D**, **E** Changes in retinal and lesion thickness post-treatment ($n = 47/50$). Mean ± SEM, $P = < 0.0001$, 0.0003 (two-way ANOVA, Sidak's test). **F** Age of nvAMD onset in non-smoking/smoking patients ($n = 47/50$). Mean ± SEM, $P = 0.0012$ (two-tailed Student's t test). **G** FFA and CD31-stained RPE-choroid flat mounts (CNV day 7) in Ctrl and Smoke mice. **H**, **I** Quantification of leakage area ($n = 10/11$) and CNV volume ($n = 5/6$). Mean ± SEM, $P = 0.0092$, 0.0097 (two-tailed Student's t test). **J** RNA-seq in retina-choroid complex of Ctrl/Smoke mice. GO annotation shows enriched pathways ($P = 0.001$ for semaphorin receptor activity, Fisher exact test). **K** GSEA indicates enriched Sema/Plexin signaling in Smoke mice. **L** Heatmap of Sema ligands in rthe etina-choroid complex of Ctrl and Smoke mice with/without CNV (day 3). Z scores of TPM values ($n = 4/4/4/4$, * indicates Ctrl vs. Smoke difference, & indicates Ctrl vs. CNV difference, # indicates Smoke vs. Smoke + CNV difference). Mean ± SEM, $P = 0.0047$, < 0.0001, 0.022 (one-way ANOVA, Tukey's test). **M** FFA and CD31-stained RPE-choroid flat mounts of *Sema4d*$^{+/+}$ and *Sema4d*$^{-/-}$ mice with/without smoking (CNV day 7). **N**, **O** Quantification of leakage area and CNV volume ($n = 13/10/10/12$). Mean ± SEM, $P = < 0.0001$, < 0.0001, 0.9836, 0.0119, 0.0474, 0.8734 (one-way ANOVA, Tukey's test). **P** Phalloidin-stained choroid explants from *Sema4d*$^{+/+}$ and *Sema4d*$^{-/-}$ mice. **Q**, **R** Quantification of sprouting vessel length (**Q**) and area (**R**) ($n = 4/5$). Mean ± SEM, $P = 0.0007$, 0.0065 (two-tailed Student's t test). $^*P < 0.05$, $^{**}P < 0.01$, $^{***}P < 0.001$, $^{****}P < 0.0001$. Scale bars: 50 μm (G right, M lower), 80 μm (G middle, M middle), 200 μm (A, G left, M upper), 1 mm (P). Source data are provided as a Source Data file.

recombinant mouse Sema4D, we found that Sema4D treatment significantly increased choroidal sprouting (Supplementary Fig. 1N–P), further confirming that Sema4D is a positive regulator of choroidal angiogenesis.

Sema4D expressed by CD8$^+$ T cells is required for smoking-aggravated CNV

To identify the cell type responsible for the increased Sema4D expression, we analyzed single-cell RNA-seq (scRNA-seq) data of choroids from patients with nvAMD and healthy donors, sourced from a previous study[18] accessible under the entry GSE135922. Uniform manifold approximation and projection (UMAP) visualization showing *SEMA4D* was predominantly expressed by the T/NK cell cluster (Fig. 2A). Furthermore, in nvAMD patients, *SEMA4D* expression was slightly higher in nvAMD patients compared to healthy donors (Supplementary Fig. 2A). We also observed that *Sema4d* expression was changed by smoking in white blood cells (WBCs), cervical lymph nodes (CLN) and spleen, and also in brown adipose tissue (BAT) with very low expression level. This effect, however, wasn't noted in other solid organs, including the white adipose tissue (WAT), brain, and lung in smoke-exposed mice (Supplementary Fig. 2B). Sema4D is expressed in both transmembrane and secreted forms. Analyzing the serum of the mice revealed that the secreted form of Sema4D was not significantly altered by smoke exposure (Supplementary Fig. 2C). Notably, Sema4D is one of the best-characterized semaphorins expressed in the immune system[19]. As multiple types of immune cells were found to infiltrate into the CNV lesion, including CD8$^+$ T cells, CD4$^+$ T cells, B cells, NK cells, CD11b$^+$F4/80$^+$ macrophages/microglia and neutrophils[20], we further analyzed the proportions of these cells, as well as Sema4D expression, under smoke and non-smoke conditions. Our analysis revealed that at CNV day 3, the proportion of CD8$^+$ T cells (gating strategy as indicated in Supplementary Fig. 2D) was increased in smoke group (Fig. 2B and Supplementary Fig. 2E), as well as mean fluorescence intensity (MFI) of Sema4D on CD8$^+$ T cells (Fig. 2C and Supplementary Fig. 2F). In line with this, in the peripheral blood, we also discovered higher Sema4D expression on CD8$^+$ T cells of active smokers compared to non-smokers in nvAMD patients (gating strategy as indicated in Supplementary Fig. 2G) (Fig. 2D, Supplementary Fig. 2H), as well as in smoking mice (Fig. 2E and Supplementary Fig. 2I). Immunostaining in the RPE-choroid flat-mounts from CNV mice at four distinct time points (day 0 (Ctrl), 3, 7, and 14) revealed the presence of CD8$^+$ T cells in the CNV lesion (Supplementary Fig. 2J), with the number of infiltrating CD8$^+$ T cells increasing from the first 3 days after laser injury and subsequently decreasing (Supplementary Fig. 2K). RPE-choroid flat-mount staining further showed a significant increase in the infiltration of CD8$^+$ T cells in the CNV lesion after smoking, and this effect is not influenced by Sema4D knockout (Supplementary Fig. 2L, M). However, there were no significant differences neither in the proportions nor MFI of Sema4D between the smoke and non-smoke groups in the rest immune cells (gating strategy as indicated in Supplementary Fig. 3A, B), including CD4$^+$ T cells (Fig. 2B, C and Supplementary Fig. 2E, F), B cells (Supplementary Fig. 3C–F), NK cells (Supplementary Fig. 3G–J), macrophages/microglia (Supplementary Fig. 3K–N), and neutrophils (Supplementary Fig. 3O–R). This suggests that smoking only primarily influences the infiltration of CD8$^+$ T cells and the expression levels of Sema4D on these cells. Moreover, FACS analysis of splenocytes from *Sema4d*$^{+/+}$ wild-type mice showed that 100% of CD8$^+$ T cells are Sema4D$^+$, while in *Sema4d*$^{-/-}$ mice, no Sema4D could be detected (Supplementary Fig. 3S).

To investigate the role of CD8$^+$ T cells in cigarette-exposure mice, firstly, we employed *Rag1*$^{-/-}$ mice (lacking T and B cells) and *Rag1*$^{+/+}$ mice and exposed them to smoke or air, after two months, we induced CNV (Fig. 2F). Notably, a reduction in both leakage area and CNV volume was observed 7 days post-laser injury in *Rag1*$^{-/-}$ mice (Fig. 2G–J), implying a detrimental role of T and B cells in CNV progression. Intriguingly, while smoking increased the vascular leakage area and CNV volume in *Rag1*$^{+/+}$ mice, this effect was notably reduced in *Rag1*$^{-/-}$ mice (Fig. 2G–J), indicating the mediation of smoking-aggravated CNV by T and B cells. Sema4D is also expressed in B cells (Fig. 2A and Supplementary Fig. 2A), and the *Rag1*$^{-/-}$ murine model is deficient in both T cells and B cells. However, neither in the proportions of B cells nor surface expression of Sema4D on B cells were observed in the mouse retina-choroid complex samples after smoke (Supplementary Fig. 3C–F). To further exclude the involvement of B cells, we conducted flow cytometry analysis to compare the expression of Sema4D on B cells from peripheral blood samples of smoke-exposed mice and patients with nvAMD. The results showed no significant difference in Sema4D expression on B cells between smoking and non-smoking patients (Supplementary Fig. 3T, U). Similarly, there was no difference in Sema4D expression on B cells from the peripheral blood of smoke-exposed mice (Supplementary Fig. 3V, W).

To confirm that Sema4D on CD8$^+$ T cells is required for smoking-aggravated CNV, we infused *Sema4d*$^{+/+}$ and *Sema4d*$^{-/-}$ CD8$^+$ T cells into *Rag1*$^{-/-}$ mice (Fig. 2K). Immunofluorescence was used to confirm the presence of transplanted T cells at the site of injury in recipient mice (Supplementary Fig. 4A, B). Mice transplanted with *Sema4d*$^{+/+}$ CD8$^+$ T cells exhibited more severe vascular leakage and neovascularization than those transplanted with normal saline (NS) (Fig. 2L–N). While in mice transplanted with *Sema4d*$^{-/-}$ CD8$^+$ T cells, vascular leakage and CNV volume were significantly reduced compared to those transplanted with *Sema4d*$^{+/+}$ CD8$^+$ T cells (Fig. 2L–N).

To further clarify that the observed effects are attributable to Sema4D expressed by CD8$^+$ T cells, we generated CD8$^+$ T-cell-specific *Sema4d* knockout (*E8i*^{Cre}; *Sema4d*$^{fl/fl}$) mice by crossing *E8i*^{Cre} and *Sema4d*$^{fl/fl}$ mice (*Sema4d*$^{fl/fl}$ littermates were used as control). The knockout efficiency was validated by fluorescence-activated cell sorting of CD8$^+$ T cells followed by qRT-PCR analysis (Supplementary Fig. 4C). These mice were subjected to smoke exposure and CNV modeling (Supplementary Fig. 4D). Quantification of the vascular leakage area and CD31 staining of the whole-mount RPE-choroid

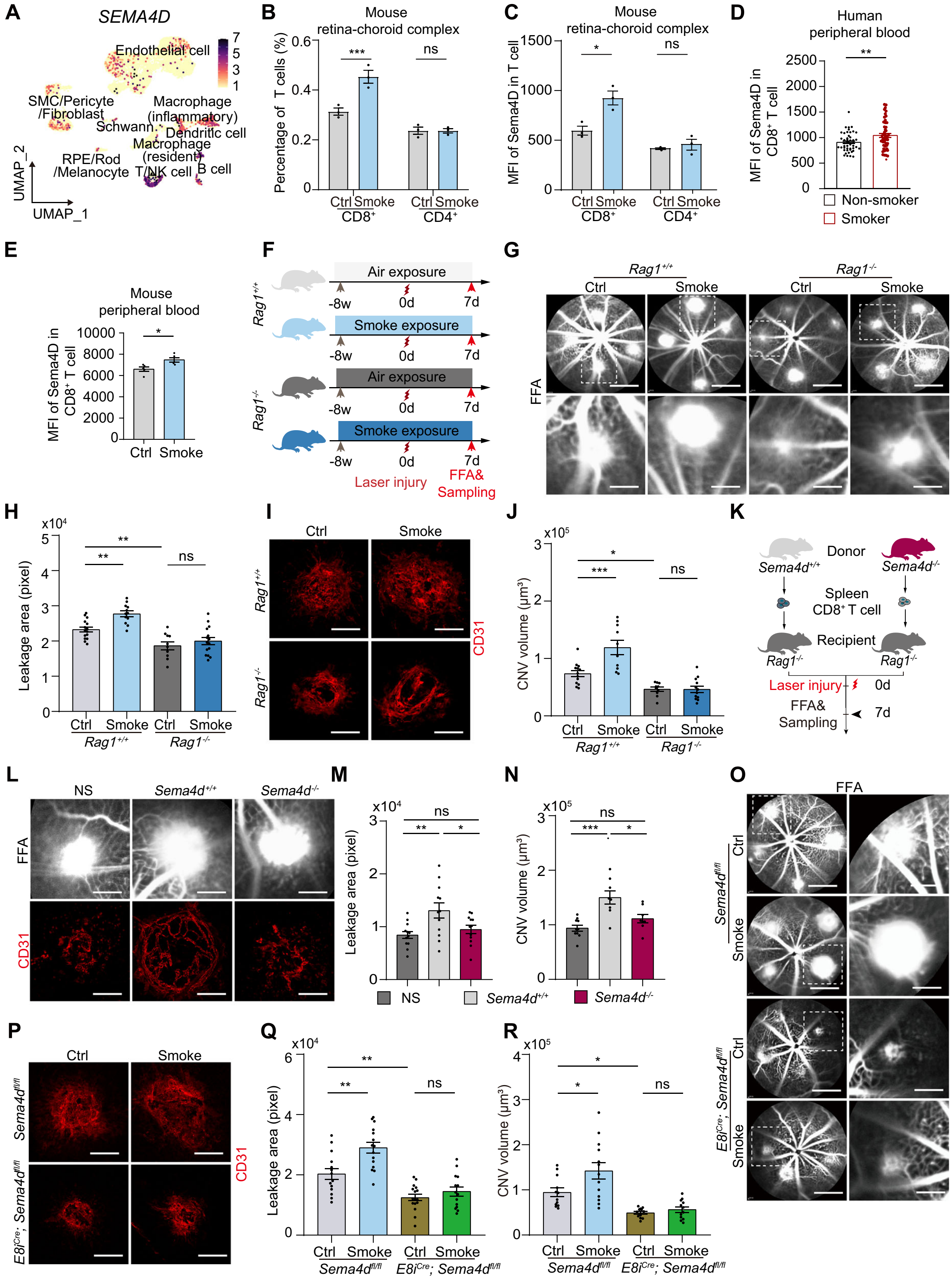

complex revealed that *Sema4d* conditional knockout in CD8$^+$ T cells significantly alleviated vascular leakage and reduced CNV volume. Furthermore, while smoking increased the vascular leakage area and CNV volume in *Sema4d*$^{fl/fl}$ mice, this effect was diminished in *E8i*^{Cre}; *Sema4d*$^{fl/fl}$ mice (Fig. 2O–R). Explants from *E8i*^{Cre}; *Sema4d*$^{fl/fl}$ CNV mice also displayed significantly reduced sprouting length and sprouting area (Supplementary Fig. 4E–G).

Collectively, these results suggest that Sema4D on CD8$^+$ T cells promotes CNV formation.

PlexinB1 expressed by pericytes mediates smoking-aggravated CNV

Next, we aimed to elucidate how increased Sema4D contributes to CNV progression. PlexinB1 is the high-affinity receptor of Sema4D[21]. By

Fig. 2 | Sema4D in CD8$^+$ T Cells Aggravates Smoking-Induced CNV. A ScRNA-seq analysis of human choroid samples from four donors. UMAP shows *SEMA4D* expression across cell types. **B**, **C** Flow cytometry analysis of CD8$^+$ and CD4$^+$ T cells in the retina-choroid complex after 8 weeks of smoking at CNV day 3 ($n = 3/3$). Mean ± SEM, $P = 0.0093$, > 0.9999, 0.0169, 0.5751 (two-tailed Student's *t* test). **D**, **E** Flow cytometry of Sema4D on CD8$^+$ T cells in peripheral white blood cells of nvAMD patients (**D**) ($n = 47/50$) and mice after 2-months smoking (**E**) ($n = 5/5$). Mean ± SEM, $P = 0.0059$, 0.0161 (two-tailed Student's *t* test). **F** Strategy for cigarette smoke exposure and CNV modeling in *Rag1*$^{+/+}$ and *Rag1*$^{-/-}$ mice. **G**, **H** Representative FFA images (**G**) and quantification of leakage area (**H**) on CNV day 7 ($n = 15/12/10/15$). Mean ± SEM, $P = 0.0059$, 0.0074, 0.7660 (one-way ANOVA, Tukey's test). **I**, **J** Representative CD31-stained RPE-choroid flat mounts images (**I**) and quantification of CNV volume (**J**) on CNV day 7 ($n = 13/10/10/12$). Mean ± SEM, $P = 0.0003$, 0.0492, > 0.9999 (one-way ANOVA, Tukey's test). **K** Diagram of CD8$^+$ T cell transfusion from *Sema4d*$^{+/+}$ or *Sema4d*$^{-/-}$ mice into *Rag1*$^{-/-}$ mice via tail vein. CNV modeling was performed, followed by FFA and CD31 staining on day 7. **L** Representative FFA and CD31-stained images of CNV mice treated as in (**K**) (NS: normal saline). **M**, **N** Quantification of leakage area ($n = 12/12/12$) and CNV volume ($n = 10/8/8$). Mean ± SEM, $P = 0.0086$, 0.0487, 0.7542, 0.0003, 0.0133, 0.3289 (one-way ANOVA, Tukey's test). **O**, **P** Representative FFA, and CD31-stained RPE-choroid flat mounts images on CNV day 7 as indicated in (Supplementary Fig. 4D). **Q**, **R** Quantification of leakage area ($n = 14/15/16/14$) and CNV volume ($n = 12/13/12/12$). Mean ± SEM, $P = 0.0016$, 0.0043, 0.7942, 0.0215, 0.0356, 0.9690 (one-way ANOVA, Tukey's test). $^*P < 0.05$, $^{**}P < 0.01$, $^{***}P < 0.001$. Scale bars: 50 μm (**I**, **L** lower, **P**), 80 μm (**G** lower, **O** right), 200 μm (**G** upper, **O** left). Source data are provided as a Source Data file.

analyzing the scRNA-seq data of choroids from patients with nvAMD and healthy donors, we found that *PLXNB1* was highly expressed by pericytes, smooth muscle cells, and fibroblasts (Fig. 3A). Since pericytes and smooth muscle cells are both mural cells that directly interact with ECs to regulate vascular function, we used a genetic lineage approach to explore the contribution of pericytes and smooth muscle cells in CNV. To trace pericyte-derived cells during CNV, we used *Pdgfrb*^{CreERT2} mice and crossed them with *Rosa26-tdTomato* reporter alleles (hereafter referred to as *Pdgfrb*^{CreERT2}*; R26-tdTom*). To trace smooth muscle cells, we used *Sm22a*^{CreERT2} or *Myh11*^{CreERT2} mice and crossed them with *Rosa26-tdTomato* reporter alleles (hereafter referred to as *Sm22a*^{CreERT2}*; R26-tdTom* or *Myh11*^{CreERT2}*; R26-tdTom*) (Fig. 3B). Upon tamoxifen-mediated genetic recombination, *Pdgfrb*-expressing pericytes, *Sm22a*-expressing smooth muscle cells, and *Myh11*-expressing smooth muscle cells were inherently labeled by *tdTomato* expression. Laser coagulation was performed after a 7-day clearing period without tamoxifen, ensuring that all recombination occurred before the insult (Fig. 3B).

Due to the melanin content in the RPE layer, fluorescence signals from tdTomato and CD31 were not detectable in the no-laser control group (Fig. 3C). We then analyzed the tdTomato$^+$ cells in the CNV lesion at three distinct time points (day 3, 7, and 14) and found that only a few tdTomato$^+$ cells could be found in *Sm22a*^{CreERT2}*; R26-tdTom* and *Myh11*^{CreERT2}*; R26-tdTom* mice. Meanwhile, a large number of tdTomato$^+$ cells were observed in the CNV lesion of *Pdgfrb*^{CreERT2}*; R26-tdTom* mice, suggesting that *Pdgfrb*-expressing pericytes are the major mural cell population contributing to CNV lesion formation (Fig. 3C, D). We also performed Ki67 staining to label proliferating cells on day 0 (Ctrl), CNV day 1, 2, 4, and 7 in the three mouse lines. Ki67 and tdTomato double-positive cells were barely detected in *Sm22a*^{CreERT2}*; R26-tdTom* and *Myh11*^{CreERT2}*; R26-tdTom* mice but were highly present in *Pdgfrb*^{CreERT2}*; R26-tdTom* mice (Supplementary Fig. 5A). The quantification also indicated that the proliferating pericytes (Ki67$^+$ tdTomato$^+$ cells) reached a high level at day 2 and day 4 and then decreased sharply (Supplementary Fig. 5B).

To confirm the contact between Sema4D on CD8$^+$ T cells and PlexinB1 on pericytes, we employed proximity ligation assay (PLA), a technique that detects protein-protein interactions in situ within a distance of less than 40 nm at endogenous protein levels[22]. CD8 was used to identify CD8$^+$ T cells, and PDGFRβ was used to identify pericytes (we used *Pdgfrb*^{CreERT2}*; Rosa26-zsGreen* reporter mice to label pericytes) (Fig. 3B). The PLA results demonstrated the association between Sema4D and PlexinB1 at the contact points between CD8$^+$ T cells and pericytes (Fig. 3E), providing further evidence of the interaction between Sema4D and PlexinB1 in these cell types.

To understand the role of PlexinB1 in pericytes when interacting with Sema4D on CD8$^+$ T cells, we transfected mouse brain vascular pericyte cells (MBVPCs) with siCtrl or *siPlxnb1* and co-cultured them with CD8$^+$ T cells isolated from spleens of wild type mice (Supplementary Fig. 5C, D). Our results showed that the expression of p-MLC, α-SMA, and COL-I was significantly reduced in the *siPlxnb1* group upon binding to Sema4D-positive CD8$^+$ T cells (Supplementary Fig. 5E, F). This indicates that *Plxnb1* expression is essential for pericyte contractility and ECM deposition signature in response to Sema4D binding.

Due to the widely reported toxic effects of Cre/CreERT recombinase in vascular development and disease-related angiogenesis[23,24], before applying pericyte-specific knockout of *Plxnb1*, we investigated the impact of the inducible *Pdgfrb*-driven CreERT recombinase in the CNV model and in retinal vascular development. The results showed no significant differences in the FFA leakage area or in the volume of choroidal neovascularization marked by CD31 between tamoxifen-treated *Pdgfrb*^{CreERT2} (*Pdgfrb*^{CreERT2}-positive) and wild-type mice (*Pdgfrb*^{CreERT2}-negative) (Supplementary Fig. 6A–D). Similarly, there was no difference in the expression of inflammatory factors, which are known to be triggered by Cre toxicity-induced DNA damages[24] (Supplementary Fig. 6E–J). Concurrently, after applying tamoxifen to newborn mice (Supplementary Fig. 6K), the vascularization of the retina was unaffected (Supplementary Fig. 6L–N). This suggests that *Pdgfrb*^{CreERT2} does not severely impair retinal angiogenesis nor affect the pathological process of CNV in our experimental conditions. Based on those results, we generated pericyte-specific PlexinB1 knockout mice by crossing *Pdgfrb*^{CreERT2} mice with *Plxnb1*$^{fl/fl}$ mice. The knockout efficiency was validated using FACS-sorted brain pericytes and confirmed by qRT-PCR (Supplementary Fig. 6O, P). To explore whether PlexinB1 expressed by pericytes contributes to smoking-aggravated CNV, we exposed *Pdgfrb*^{CreERT2}, *Plxnb1*$^{fl/fl}$, and *Plxnb1*$^{fl/fl}$ mice to smoke or filtered air. Two months later, we induced CNV (Fig. 3F). A reduction in leakage area and CNV volume was observed 7 days after laser injury in *Pdgfrb*^{CreERT2}; *Plxnb1*$^{fl/fl}$ mice exposed to air, suggesting that inhibiting PlexinB1 in pericytes alleviates CNV progression (Fig. 3G–I). Moreover, while smoking increased the vascular leakage area (Fig. 3H), CNV volume (Fig. 3I) and PDGFRβ positive pericyte area (Supplementary Fig. 6Q) in *Plxnb1*$^{fl/fl}$ mice, the effect was diminished in *Pdgfrb*^{CreERT2}; *Plxnb1*$^{fl/fl}$ mice, further indicating that pericyte PlexinB1 mediates smoking-aggravated CNV.

Pericytes signature characterization in smoke-related CNV

During pathophysiological processes, pericytes become activated and display altered marker profiles, including α-SMA, RGS5, NG2, and PDGFRβ. They detach from the basement membrane, leading to increased vessel permeability, and undergo transdifferentiation into myofibroblasts, resulting in the deposition of collagenous extracellular matrix[25]. To better characterize the changes in pericytes under CNV and smoking conditions, we performed scRNA-seq of retina-choroid complexes from smoke-exposed mice and air-exposed mice with or without CNV. Among the 47,053 cells (11,299 cells from control, 10,608 cells from CNV, 13,737 cells from smoke, 11,409 cells from smoke-exposed CNV mice), we classified the cell clusters based on the expression of cell type-specific marker genes (Fig. 4A). UMAP

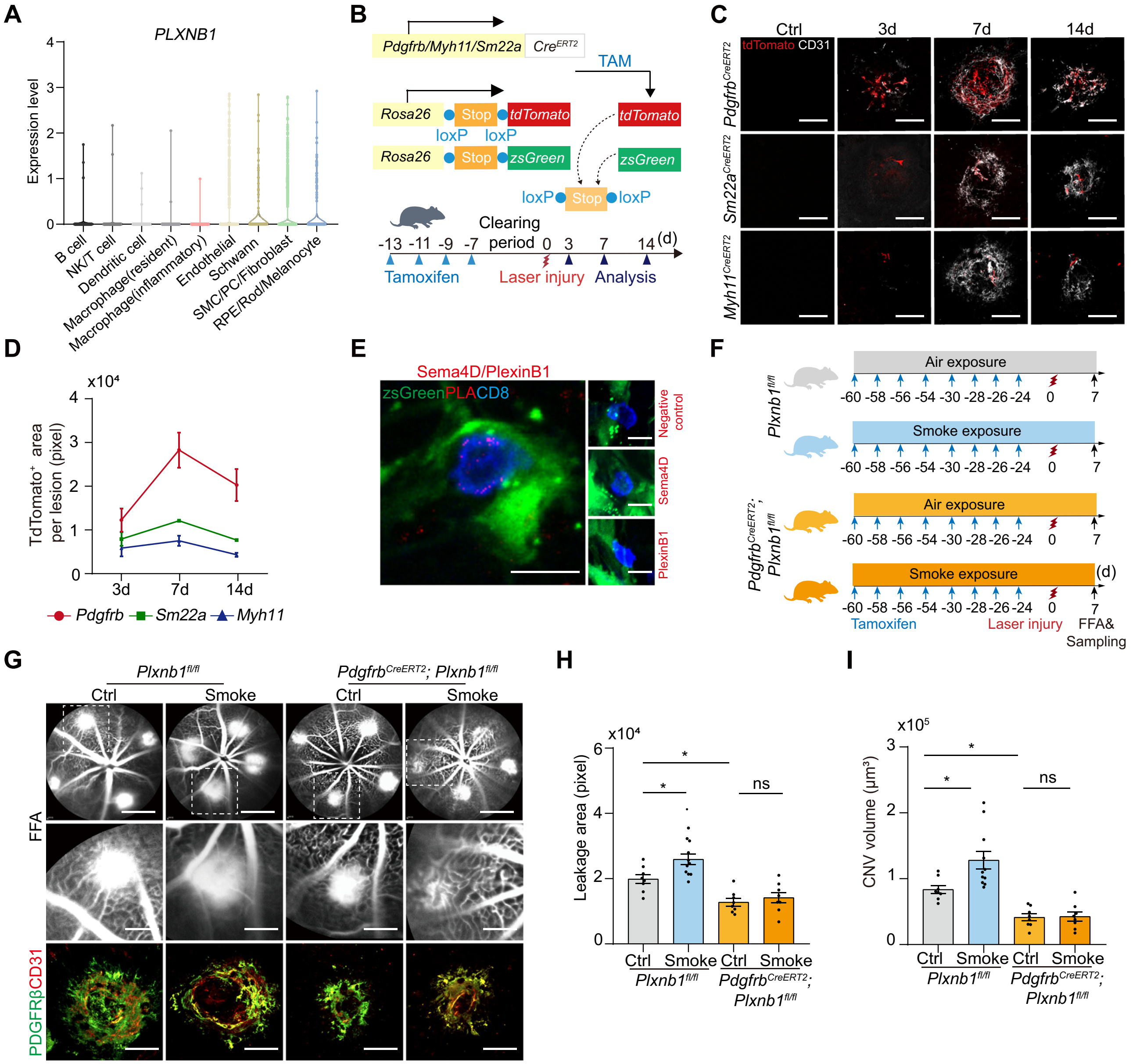

Fig. 3 | PlexinB1 expressed by pericytes mediates smoking-aggravated CNV. **A** Human choroid scRNA-seq analysis showing that *PLXNB1* was expressed across different cell types. The width of the violin indicates the probability density of the data at different values. **B** Schematic illustrates the breeding strategy and CNV modeling for lineage-tracing mice. *Pdgfrb*^{CreERT2}, *Sm22a*^{CreERT2} or *Myh11*^{CreERT2} mice were crossed with *Rosa26-tdTomato* or *Rosa26-zsGreen* reporter alleles to generate *Pdgfrb*^{CreERT2}*; R26-tdTom*, *Pdgfrb*^{CreERT2}*; R26-zsGreen*, *Sm22a*^{CreERT2}*; R26-tdTom*, and *Myh11*^{CreERT2}*; R26-tdTom mice.* After four consecutive intraperitoneal injections of tamoxifen, followed by a one-week clearing period, CNV was induced. The RPE-choroid flat mounts were harvested for analysis at 3, 7, and 14 days. **C** Representative confocal images showing RPE-choroid flat mounts stained for CD31 (white) and tdTomato (red) from CNV mice at indicated time points. **D** Quantification of tdTomato positive area within CNV lesions of (**C**): *Pdgfrb*^{CreERT2}*; R26-tdTom* ($n = 5/4/4$ at day 3, 7, and 14, respectively), *Sm22a*^{CreERT2}*; R26-tdTom* ($n = 4/5/5$ at days 3, 7, and 14, respectively), and *Myh11*^{CreERT2}*; R26-tdTom* ($n = 5/4/4$ at day 3, 7, and 14, respectively). Mean ± SEM. **E** PLA analysis showing the interaction of Sema4D and PlexinB1 in CNV lesion of *Pdgfrb*^{CreERT2}*; ZsGreen* mice. CD8 staining was used to label CD8^{+} T cells. Negative control was performed by omitting primary antibodies, Sema4D control, and PlexinB1 control were performed by using a single primary antibody. **F** Schematic illustrates tamoxifen administration, smoking exposure, and CNV modeling in *Plxnb1*$^{fl/fl}$ and *Pdgfrb*^{CreERT2}*; Plxnb1*$^{fl/fl}$ mice. **G** Representative FFA images (upper) and confocal images of RPE-choroid flat mounts (lower) from mice treated as in (**F**). Pericytes were labeled by PDGFRβ (green), and neovascular was labeled by CD31 (red). **H, I** Quantification of leakage area (**H**) ($n = 8/11/8/8$) and CNV volume (**I**) ($n = 8/11/8/8$) of (**G**). Mean ± SEM, $P = 0.0294$, 0.0158, 0.9205, 0.0131, 0.0324, 0.9998 (one-way ANOVA, Tukey's test). * $P < 0.05$, ** $P < 0.01$. Scale bars: 10 μm in (**E**), 50 μm in (**C**, **G** lower), 80 μm in (**G** middle), 200 μm in (**G** upper). Source data are provided as a Source Data file.

visualization showed that vascular mural cells and fibroblasts could be divided into seven distinct clusters: pericyte cluster 1-3, fibroblast cluster 1-3, and vascular smooth muscle cells (Fig. 4B). Upon comparing the four treatment groups, we observed an increased percentage of pericyte cluster 3 in CNV mice compared to control mice, and smoke exposure further increased this population (Fig. 4C). We also analyzed immune cell populations and identified nine distinct subclusters: T cells, B cells, NK cells, macrophage, microglia, monocytes, mast cells, neutrophils, and dendritic cells (Supplementary Fig. 7A).

Gene expression patterns and gene ontology (GO)-biological processes of the three pericyte clusters indicated that the pericyte_1 cluster highly express cytokines, including *Cxcl1*, *Cxcl10*, and *Cxcl12*,

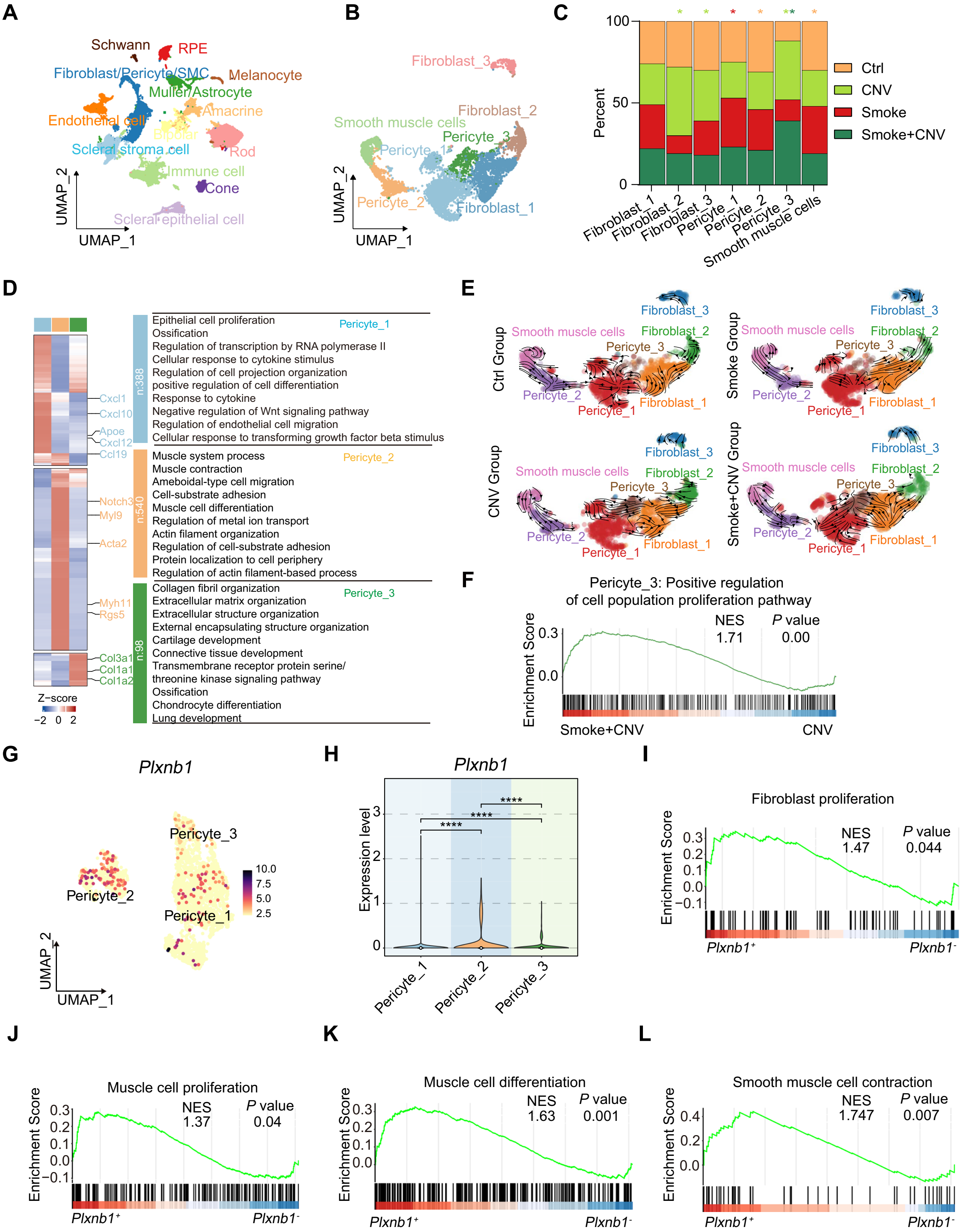

pericyte_2 cluster demonstrate higher expression of genes associated with cell contractility such as *Acta2*, and pericyte_3 with strong expression of many genes associated with ECM components, such as *Col1a1* and *Col1a2* (Fig. 4D). Gene set variation analysis (GSVA) analysis also revealed that pericyte_1 displayed the highest score in cytokine-mediated signaling, pericyte_2 with positive GSVA score enrichment for features associated with contractility, and pericyte_3 showed fibroblast proliferation (Supplementary Fig. 7B–D). GSEA further illustrated significant enrichments in cytokine production signatures in pericyte_1, muscle contraction in pericyte_2, and fibroblast activation in pericyte_3 among smoke-exposed mice in both CNV and control conditions (Supplementary Fig. 7E–J). Notably, smoking led to increased myofibroblast and ECM deposition features, including p-MLC, α-SMA, and COL-I in the CNV lesion (Supplementary Fig. 7K). As

Fig. 4 | Pericytes characteristics in CNV. A, **B** ScRNA-sequencing analysis conducted in the retina-choroid complex of Ctrl and Smoke mice after a two-month smoking period with or without CNV modeling. After filtration, a total of 47,083 cells were included (**A**). Specific cell types exhibited varying cell counts: 1438 cells for fibroblast_1, 510 cells for fibroblast_2, 304 cells for fibroblast_3, 2,211 cells for pericyte_1, 618 cells for pericyte_2, 402 cells for pericyte_3, and 431 cells for smooth muscle cells (**B**). **C** The contribution of the four experimental groups to each cluster is visualized with a stacked bar chart. Hypergeometric distribution analysis was performed to quantify if an experimental condition was significantly enriched in each cluster (asterisks). Asterisks are colored according to experimental conditions and placed above a cluster if the enrichment test was significant at the $\alpha = 0.05$ level after Bonferroni correction. $P = < 0.0001$, 0.0288, < 0.0001, 0.0017, < 0.0001, < 0.0001, 0.0229. **D** Heatmap displays the expression of discriminative genes per cluster. Top significantly enriched biological process GO terms are presented for each cluster. **E** Visualizes RNA velocity based on the UMAP. Arrows represent the local average velocity in the vector field, indicating the fate and speed of differentiation events in these cells. **F** GSEA highlighting the positive regulation of cell population proliferation pathway enriched in smoke-exposed CNV mice compared with CNV mice. **G** and **H** Expression of *Plxnb1* in different pericytes populations from mouse scRNA-seq data. The width of the violin indicates the probability density of the data at different values. $P = < 0.0001$, < 0.0001, < 0.0001 (one-way ANOVA, Tukey's test). **I**–**L** GSEA showing fibroblast proliferation pathway (**I**), muscle cell proliferation pathway (**J**), muscle cell differentiation pathway (**K**), smooth muscle contraction pathway (**L**) enriched in *Plxnb1*$^+$ pericytes compared with *Plxnb1*$^-$ pericytes. **** $P < 0.0001$. One-way ANOVA followed by Tukey's multiple comparisons test in (**H**). Source data are provided as a Source Data file.

we observed an increased proportion of pericyte_3 due to CNV and smoke exposure, we performed RNA velocity analysis on the four groups of single-cell sequencing data. In the Smoke + CNV group, there was a clear transition from Pericyte_3 to Fibroblast_1, which was not seen in the other groups. Moreover, our analysis showed that no other cell type transitioned into Pericyte_3 across all groups (Fig. 4E). As GSVA analysis showed that pericyte 3 had the highest score in fibroblast proliferation (Supplementary Fig. 7D), and GSEA displayed a notable enrichment in the positive regulation of cell proliferation signature in smoke-exposed mice under both CNV (Fig. 4F) and Ctrl (Supplementary Fig. 7L) conditions, indicating the likelihood that the expanded population of pericyte_3 in CNV and smoke exposure might result from cell proliferation.

To assess the relevance in human disease conditions, we also performed this analysis using scRNA-seq data of choroids from patients with nvAMD and healthy donors. Pericyte clusters 1–4, fibroblast clusters 1–3, and vascular smooth muscle cells were divided and visualized using UMAP (Supplementary Fig. 7M). All four pericyte clusters showed an increased percentage in patients with nvAMD compared with healthy donors, with cluster 3 showing the highest fold induction (Supplementary Fig. 7N). GO-biological processes of the four pericyte clusters indicated that while pericyte cluster 4 exhibited apoptosis and cell death features, the other three clusters (clusters 1–3) showed similar features as the mouse data (Supplementary Fig. 7O).

UMAP showed that all three pericyte clusters express *Plxnb1*, with Cluster 2 exhibiting the highest level (Fig. 4G, H). To investigate whether *Plxnb1*$^+$ pericytes in CNV are transitioning into myofibroblasts, we divided the pericytes into two subgroups: *Plxnb1*$^+$ and *Plxnb1*$^-$. GSEA revealed that pathways related to fibroblast proliferation (Fig. 4I), muscle cell proliferation (Fig. 4J), muscle cell differentiation (Fig. 4K), and smooth muscle contraction (Fig. 4L) were significantly enriched in *Plxnb1*$^+$ pericytes. These findings suggest that in the CNV model, *Plxnb1*$^+$ pericytes are more likely to undergo transformation into myofibroblasts.

PlexinB1 regulates pericytes activation and vascular stability

Loss of *Plxnb1* in pericytes significantly reduced myofibroblasts/ECM deposition features p-MLC, α-SMA and COL-I in the CNV lesion (Fig. 5A). To further validate the role of PlexinB1 in pericytes in vitro, we knocked down *PLXNB1* using siRNA in primary human brain vascular pericytes (HBVPCs) (Supplementary Fig. 8A, B) and found that this significantly reduced the expression of p-MLC, α-SMA and COL-I with or without Sema4D stimulation (Fig. 5B, C). The transdifferentiated pericytes with myofibroblast features also contribute to the ECM remodeling[25]. The collagen gel contraction assay is a widely used method to investigate cell-ECM interactions in 3D environments, providing insight into cellular contractility in a three-dimensional context[26]. Using this assay, we observed that Sema4D treatment significantly increased gel contraction. In contrast, *PLXNB1* knockdown significantly reduced gel contraction and diminished the effect of Sema4D (Fig. 5D, E). A scratch migration assay also indicated that Sema4D increased pericyte migration, while *PLXNB1* knockdown diminished this effect (Supplementary Fig. 8C, D). Moreover, the ex vivo explant system further proved that while Sema4D stimulus increased sprouting in *Plxnb1*$^{fl/fl}$ mice, the effect was diminished in *Pdgfrb*^{CreERT2}; *Plxnb1*$^{fl/fl}$ mice (Fig. 5F–H).

In the CNV lesion at day 7, we found that CD8$^+$ T cells are in contact with pericytes (labeled as PDGFRβ) (Fig. 5I). To further demonstrate that CD8$^+$ T cells derived Sema4D signals to pericytes for activation, we sorted CD8$^+$ T cells from *Sema4d*$^{-/-}$ and *Sema4d*$^{+/+}$ mice and cultured them with MBVPCs (Fig. 5J). The expression of p-MLC, α-SMA, and COL-I was significantly lower in pericytes co-cultured with CD8$^+$ T cells from *Sema4d*$^{-/-}$ mice (Fig. 5K–N). Consequently, pericytes co-cultured with CD8$^+$ T cells from *Sema4d*$^{-/-}$ mice exhibited reduced gel contraction and migration compared to those co-cultured with CD8$^+$ T cells from *Sema4d*$^{+/+}$ mice (Supplementary Fig. 8E–H).

Pericytes communicate with ECs and play a crucial role in stabilizing blood vessels[27,28]. CellChat analysis between ECs and pericytes revealed that smoking indeed altered their signaling interactions (Fig. 5O). To understand whether PlexinB1 regulates pericytes for vessel stability, we utilized a microfluidic chip-based, lumenized vascular network containing only ECs and pericytes (Fig. 5P)[29]. HBVPCs were transfected with scramble or *PLXNB1* siRNA and co-cultured with human umbilical vein endothelial cells (HUVECs) in the microfluidic chips for 10 days to facilitate the formation of a pericyte-covered vascular network. Sema4D stimulation led to increased vascular leakage, as evidenced by the accumulation of fluorescent microbeads in the extravascular space (Fig. 5Q, R). Meanwhile, we observed significant morphological changes in pericytes upon Sema4D treatment, characterized by the loss of elongated cytoplasmic processes and the formation of lamellipodia. These alterations imply that pericytes acquired a migratory phenotype. However, the knockdown of *PLXNB1* impeded pericyte retraction and restricted the vascular leakage induced by Sema4D (Fig. 5S).

ROR2 mediates PlexinB1 phosphorylation and activation in pericytes

PlexinB1 contains a carboxy-terminal PDZ domain interaction motif through which it binds to the RHO guanine nucleotide exchange factors (GEFs) 11 and 12 (also known as PDZ RHOGEF and LARG, respectively)[30–32]. The PlexinB–RHOGEF complex mediates semaphorin-induced RhoA activation to regulate many cellular responses. It is known that PlexinB1 forms a receptor complex with either erythroblastic leukemia viral oncogene homolog 2 (ErbB2)[33] or hepatocyte growth factor receptor (c-Met)[34], two receptor tyrosine kinases required for downstream signaling regulation in other cell types. We first determined whether ErbB2 and c-Met also interact with PlexinB1 in pericytes. We constructed AdC68-Flag-PlexinB1 and infected HBVPCs, followed by Sema4D stimulation. Afterward, co-

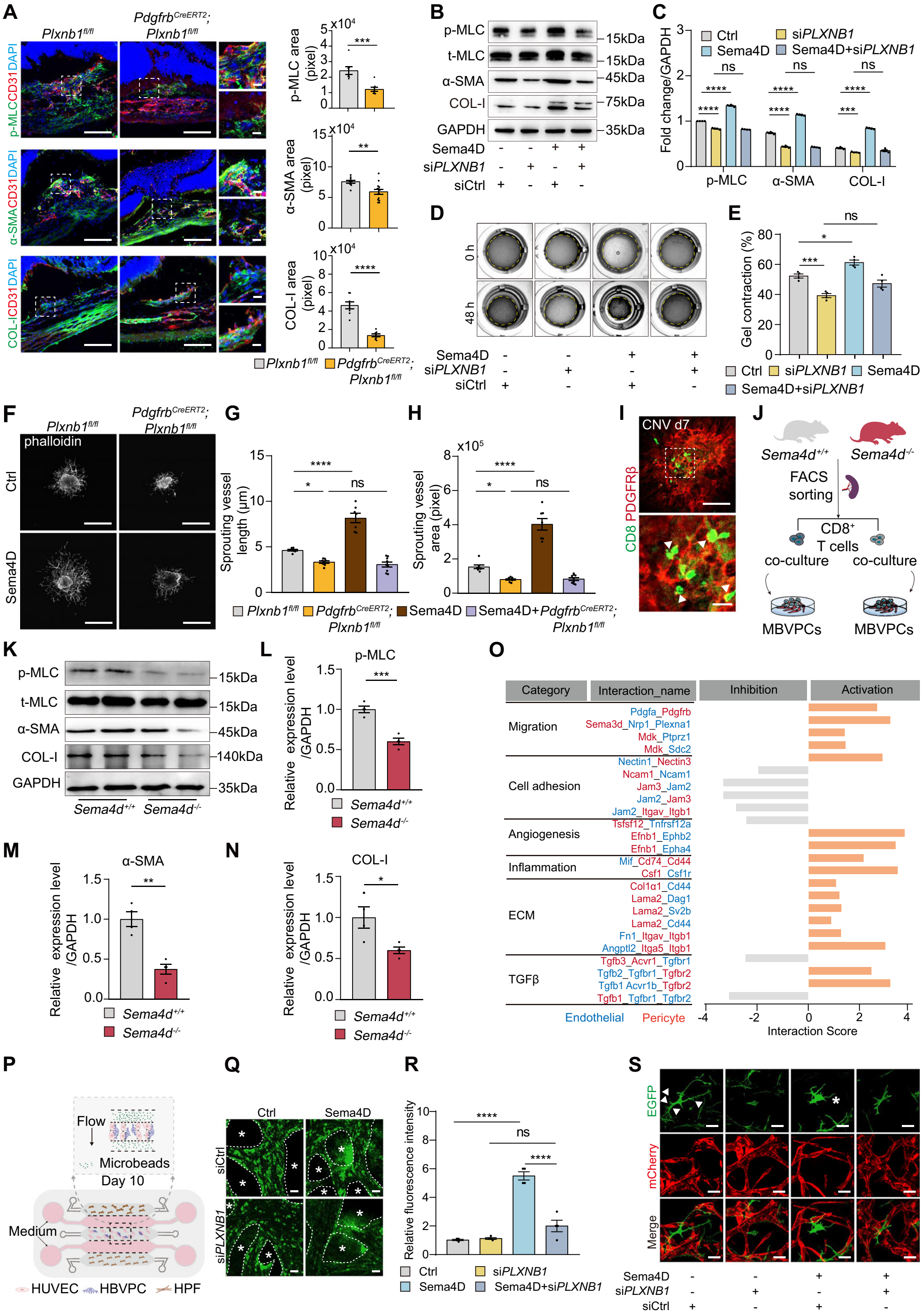

immunoprecipitation (CO-IP) analysis of Flag-PlexinB1 and endogenous ErbB2 and c-Met was performed. We did not detect any binding toward ErbB2 and c-Met in pericytes (Fig. 6A), suggesting that alternative receptor tyrosine kinases are involved as co-receptors of PlexinB1 in pericytes.

To identify the associating kinase receptor, HBVPCs infected with AdC68-Flag-PlexinB1 were stimulated with Sema4D, and PlexinB1 was immunoprecipitated with anti-Flag beads from cell lysates for mass spectrometry. We found that ARHGEF11 and 12 were identified as PlexinB1 binding proteins (Fig. 6B). Interestingly, receptor tyrosine kinase-like orphan receptor 2 (ROR2) was identified as the only receptor tyrosine kinase associated with PlexinB1 in pericytes (Fig. 6B). ROR2 is highly expressed in fibroblast, smooth muscle cells and pericytes in both human and mouse samples (Supplementary Fig. 9A, B).

Fig. 5 | PlexinB1 on Pericytes Mediates Smoking-Aggravated CNV. **A** Immunofluorescence staining of frozen eye sections from *Plxnb1*$^{fl/fl}$ and *Pdgfrb*^{CreERT2}*; Plxnb1*$^{fl/fl}$ mice. p-MLC/α-SMA/COL-I (green), CD31 (red), and DAPI (blue) were stained. Quantification of p-MLC ($n = 6/8$), α-SMA ($n = 8/12$), and COL-I ($n = 8/7$). Mean ± SEM, $P = 0.0005$, 0.0017, < 0.0001 (two-tailed Student's *t* test). **B**, **C** HBVPCs transfected with siCtrl or *siPLXNB1* and treated with Sema4D or vehicle. Representative blots (**B**) and quantification (**C**) of p-MLC/α-SMA/COL-I expression ($n = 4/4/4/4$). Mean ± SEM, $P = < 0.0001$, < 0.0001, 0.4917, < 0.0001, < 0.0001, 0.8724, 0.0008, < 0.0001, 0.1785 (one-way ANOVA, Tukey's test). **D**, **E** Contracted gel (**D**) and quantification (**E**) of HBVPCs treated as in (**B**) ($n = 4/4/4/4$). Mean ± SEM, $P = 0.0007$, 0.0389, 0.0944 (one-way ANOVA, Tukey's test). **F** Laser-induced choroid explants from *Plxnb1*$^{fl/fl}$ and *Pdgfrb*^{CreERT2}*; Plxnb1*$^{fl/fl}$ mice stimulated with Sema4D or vehicle. Representative confocal images of phalloidin-stained explants. **G**, **H** Quantification of sprouting vessel length (**G**) and area (**H**) ($n = 7/7/8/9$). Mean ± SEM, $P = 0.0218$, < 0.0001, 0.9037, < 0.0269, < 0.0001, 0.9993 (one-way ANOVA, Tukey's test). **I** RPE-choroid flat mounts showing CD8$^+$ T cells and pericytes on CNV day 7. **J** Scheme of co-culture of CD8$^+$ T cells (from *Sema4d*$^{+/+}$ or *Sema4d*$^{-/-}$ mice) and MBVPCs for 48 h. **K**–**N** Representative blots (**K**) and quantification of p-MLC/α-SMA/COL-I (**L**–**N**) in MBVPCs treated as in (J) ($n = 4/4$). Mean ± SEM, $P = 0.0004$, 0.0013, 0.0255 (two-tailed Student's *t* test). **O** Changes in pericyte-endothelial cell interactions in CNV and CNV+Smoke groups. The bar graph shows interaction probability. **P** Schematic of vascular leakage assay in microfluidic chips. **Q**, **R** Representative images (Q) and quantification (R) of leaked FITC-microbeads in ECM (asterisks) ($n = 6/6/6/6$). Mean ± SEM, $P = < 0.0001$, 0.1209, < 0.0001 (one-way ANOVA, Tukey's test). **S** Representative images of the vascular network. Arrowheads indicate pericyte cellular processes, asterisk indicates detached pericyte. $^*P < 0.05$, $^{**}P < 0.01$, $^{***}P < 0.001$, $^{****}P < 0.0001$. Scale bars: 5 μm (A right, I lower), 50 μm (**A** left, middle, **I** upper, **Q**, **S**), 1 mm (**F**). Source data are provided as a Source Data file.

To validate this result, we performed CO-IP analysis of Flag-PlexinB1 and endogenous ROR2 in HBVPCs, with or without Sema4D stimulation. We found that PlexinB1 indeed associates with ROR2, and this association is enhanced upon Sema4D stimulation (Fig. 6C). Furthermore, the phosphorylation of PlexinB1 was enhanced after Sema4D stimulation (Fig. 6D). Importantly, when we knocked down *ROR2*, the phosphorylation of PlexinB1 was substantially reduced, suggesting that ROR2 serves as an associating kinase (Fig. 6D). PlexinB1 can bind activated RhoA upon stimulation by Sema4D[35]. We also found that the interaction between PlexinB1 and RhoA was enhanced by Sema4D stimulation (Fig. 6E). Consequently, the activity of RhoA was increased by Sema4D stimulus in pericytes, and this effect was diminished when *PLXNB1* (Supplementary Fig. 8A, B) or *ROR2* (Supplementary Fig. 9C, D) was knocked down (Fig. 6F). We also used isolated CD8$^+$ T cells from both *Sema4d*$^{+/+}$ and *Sema4d*$^{-/-}$ mice and co-cultured with MBVPCs as we did in (Fig. 5J). RhoA activity was also reduced in *Sema4d*$^{-/-}$ T cells co-cultured MBVPCs (Fig. 6G).

To further prove Sema4D-PlexinB1 inhibits pericyte activation through ROR2 and RhoA, we utilized Ozuriftamab (a human IgG1 kappa antibody specifically targeting ROR2) to inhibit ROR2 and Rhosin hydrochloride (a specific RhoA GTPase inhibitor) to inhibit RhoA GTPase. Our results showed that Sema4D treatment increased the expression of p-MLC, α-SMA, and COL-I, while the presence of Ozuriftamab or Rhosin hydrochloride significantly reduced these effects (Fig. 6H–K). These results further confirmed the role of ROR2 and RhoA in the Sema4D-mediated pericyte activation.

CXCL12-CXCR4 signaling mediates T cell recruitment in CNV

To explore the signaling that mediates T cell recruitment in CNV, we first analyzed our scRNA-seq data for cytokine signaling related to T cell recruitment. Interestingly, UMAP indicated that, while the immune cell population showed high expression of T cell recruitment cytokine signaling as expected, the pericyte population also exhibited a high expression (Fig. 7A). This suggested that pericytes might contribute to the recruitment of T cells. To dissect the specific signaling, we performed a cell-cell communication analysis using CellChat. The results revealed that the pericyte-to-CD8$^+$ T cell signal pair CXCL12-CXCR4 interaction was enhanced in the CNV group (Fig. 7B, C). CXCL12-CXCR4 is known as a T cell chemotaxis pathway[36,37]. Interestingly, UMAP indicated that *CXCL12* was not highly expressed by the immune cell population but was abundantly expressed by pericytes in both mouse (Supplementary Fig. 10A, B) and human samples (Supplementary Fig. 10C, D), while the receptor CXCR4 was highly expressed by immune cells, including T cells (Supplementary Fig. 10E–G). ELISA of vitreous samples from CNV and control mice exposed to smoke or air showed that CNV increased the level of CXCL12, and smoke exposure further increased it (Fig. 7D).

Next, we aimed to test whether blocking the CXCL12-CXCR4 interaction could inhibit T cell infiltration and thus inhibit CNV. Plerixafor, a selective antagonist of CXCR4, was administered to smoke or air-exposed CNV mice (Fig. 7E). Smoking alone significantly increased CXCR4$^+$ CD8$^+$ T cell infiltration in the retina-choroid complex, as indicated by flow cytometry analysis, while this could be efficiently inhibited by Plerixafor (Fig. 7F and Supplementary Fig. 10H). Consequently, Plerixafor significantly reduced vascular leakage area and CNV volume and diminished the effect of smoke exposure (Fig. 7G–J). To evaluate the effect of Plerixafor on pericytes, we stained PDGFRβ for pericytes and α-SMA for activated pericytes. CD8 staining was also performed to label CD8$^+$ T cells. Quantification showed that consistent with the data on vascular leakage area and CNV volume, Plerixafor significantly reduced both PDGFRβ and α-SMA positive areas, as well as the number of CD8$^+$ T cells, effectively counteracting the effects of smoke exposure (Supplementary Fig. 10I–M).

As CXCR4 is expressed by various immune cells (Supplementary Fig. 10E–G), we also analyze the presence of other immune cells in the retina-choroid complex following CNV induction and Plerixafor treatment (Supplementary Fig. 11A). The results indicated that Plerixafor had no significant effect on the infiltration of B cells, NK cells or neutrophils after CNV (Supplementary Fig. 11B–G). However, we observed a significant inhibitory effect on macrophage/microglia infiltration (Supplementary Fig. 11H, I), which aligns with existing knowledge that CXCR4 is critical for macrophage chemotaxis[38].

To further demonstrate that the observed effects of smoking-induced aggravation of the CNV phenotype are specifically due to CD8$^+$ T cell infiltration via the CXCL12/CXCR4 axis, we generated CD8$^+$ T-cell-specific CXCR4 knockout (*E8i*^{Cre}; *Cxcr4*$^{fl/fl}$) mice by crossing *E8i*^{Cre} with *Cxcr4*$^{fl/fl}$ mice. The knockout efficiency was validated by fluorescence-activated cell sorting of CD8$^+$ T cells (Supplementary Fig. 2D) followed by qRT-PCR analysis (Supplementary Fig. 11J). These mice were subjected to smoke exposure and CNV modeling (Fig. 7K). In *Cxcr4*$^{fl/fl}$ mice, smoking exacerbated vascular leakage and neovascularization; however, this effect was significantly reduced in *E8i*^{Cre}; *Cxcr4*$^{fl/fl}$ mice (Fig. 7L–O). This finding suggests that CD8$^+$ T cell infiltration via the CXCL12/CXCR4 axis plays a crucial role in mediating smoking-induced aggravation of the CNV phenotype.

Targeting Sema4D alleviates CNV progression and enhance anti-VEGF therapy

To explore whether T cell-expressed Sema4D contributes to the progression of nvAMD and might affect the responsiveness to anti-VEGF therapy, we analyzed the expression of Sema4D on CD8$^+$ T cells from the blood samples of nvAMD patients who received 3 + PRN anti-VEGF therapy. A significant correlation was found between the lesion recovery rate and the Sema4D expression level on CD8$^+$ T cells in patients with nvAMD (Fig. 8A–C).

To determine the therapeutic potential of inhibiting Sema4D-PlexinB1 signaling in nvAMD, we used a mouse Sema4D-specific neutralizing antibody to see whether it could suppress CNV and enhance

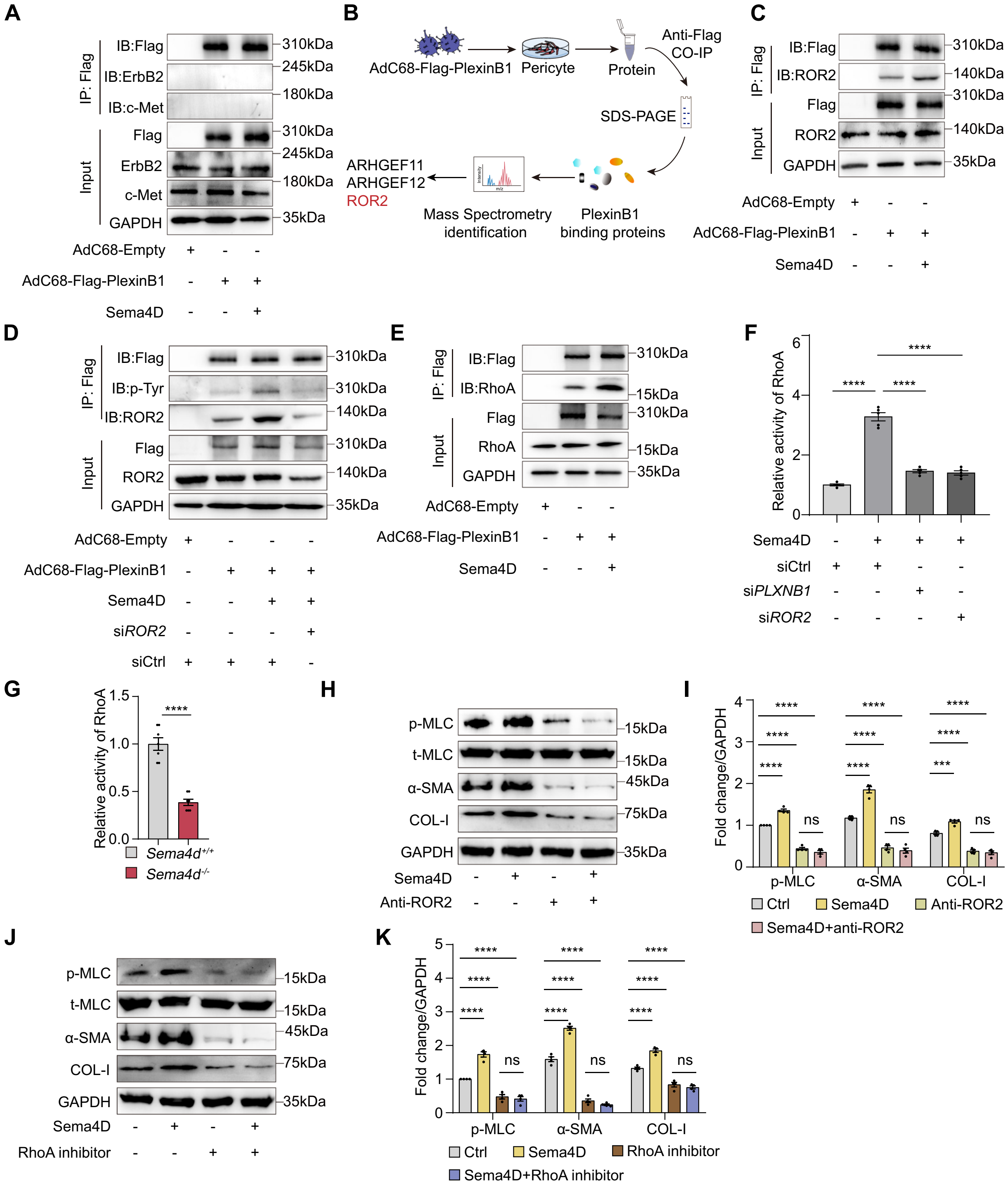

anti-VEGF (we used Conbercept, an anti-VEGF agent used for treating nvAMD in clinics) treatment efficacy. A safety test through OCT examination and TUNEL staining showed that the treatment led to no obvious toxicity in the retina (Supplementary Fig. 12A–C). There were also no significant changes in the function of the eyes, as evaluated by ERG (Supplementary Fig. 12D–K). By analyzing vascular leakage and CNV formation, we found that anti-Sema4D had a clear protective effect, comparable to that of Conbercept (Fig. 8D, E). Importantly, when Conbercept and anti-Sema4D were combined, the protective effect became more robust and was significantly better than that of Conbercept or anti-Sema4D alone (Fig. 8D, E). We also evaluated whether the therapy affect the activation of pericytes and found that Conbercept and anti-Sema4D treatment alone both reduced the expression of p-MLC, α-SMA, and COL-I, while combining Conbercept and anti-Sema4D resulted in a significantly stronger reduction, as assessed by western blot and immunostaining (Fig. 8F–I). We further analyzed CD8$^+$ T cell content under these treatment conditions. CD8 and α-SMA staining of the whole-mount RPE-choroid complex revealed that the number of CD8$^+$ T cells was reduced in both the Conbercept and the combination treatment groups, but anti-Sema4D

Fig. 6 | ROR2 is Required for PlexinB1 Phosphorylation and Activation in Pericytes. A HBVPCs infected with Flag-PlexinB1 adenovirus and stimulated with Sema4D (1.6 μg/mL) for 30 min. PlexinB1 interactions with ErbB2 or c-Met were detected by CO-IP and immunoblot. Blots represent three independent experiments. **B** HBVPCs infected with Flag-PlexinB1 adenovirus and treated with Sema4D. Mass spectrometry identified ARHGEF11, ARHGEF12, and ROR2 were interacted with Flag-PlexinB1. **C** Representative blots of CO-IP of Flag-PlexinB1 with ROR2 in HBVPCs stimulated with Sema4D (1.6 μg/mL) for 30 min. **D** HBVPCs were infected with Flag-PlexinB1 and transfected with siCtrl or *siROR2*, then treated with Sema4D or vehicle. PlexinB1 phosphorylation was detected by pan-phospho-tyrosine (p-Tyr) antibody. CO-IP of Flag-tagged PlexinB1 with ROR2 was also shown. Blots represent three independent experiments. **E** Representative blots of CO-IP of Flag-PlexinB1 with RhoA in HBVPCs stimulated with Sema4D (1.6 μg/mL) for 30 min. **F** G-LISA for GTP-bound RhoA displayed that Sema4D-induced RhoA activation was diminished after knockdown of *ROR2* or *PLXNB1* using siRNA in pericytes ($n = 5/5/5/5$). Mean ± SEM, $P < 0.0001$ (one-way ANOVA, Tukey's test). **G** G-LISA for GTP-bound RhoA displayed that RhoA activity was lower in MBVPCs after co-cultured with *Sema4d*$^{-/-}$ CD8$^+$ T cell compared with *Sema4d*$^{+/+}$ CD8$^+$ T cell treated group ($n = 7/7$). Mean ± SEM, $P < 0.0001$ (two-tailed Student's t test). **H**, **I** HBVPCs were stimulated with Sema4D (1.6 μg/mL) for 8 h in the presence or absence of RhoA inhibitor Rhosin hydrochloride (40 μM). Representative blots (**H**) and quantification (**I**) of p-MLC, α-SMA, and COL-I ($n = 4/4/4/4$). Mean ± SEM, $P < 0.0001$ (one-way ANOVA, Tukey's test). **J**, **K** HBVPCs stimulated with Sema4D (1.6 μg/mL) for 8 h in the presence or absence of RhoA inhibitor Rhosin hydrochloride (40 μM). Representative blots (**J**) and quantification (**K**) of *p*-MLC, α-SMA, and COL-I ($n = 4/4/4/4$) are shown. Mean ± SEM, $P < 0.0001$ (one-way ANOVA, Tukey's test). $^{***}P < 0.001$, $^{****}P < 0.0001$. Source data are provided as a Source Data file.

treatment did not significantly affect the infiltration of CD8$^+$ T cells in CNV lesion. (Supplementary Fig. 13A, B). These results suggest that anti-Sema4D treatment reduced vascular leakage, CNV formation, and pericyte activation, but not CD8$^+$ T cell recruitment, suggesting that anti-VEGF and anti-Sema4D function through distinct mechanisms.

To further illustrate the effectiveness of the combined treatment, we employed low-density lipoprotein receptor (VLDLR) knockout mice (*Vldlr*$^{-/-}$ mice), which exhibit characteristics of retinal angiomatous proliferation and choroidal neovascularization. These features resemble the neovascularization observed in conditions like macular telangiectasia and nvAMD. In these mice, neovascularization extends from the deep layer of the retinal vasculature into the outer plexiform layer at postnatal day 12 (P12), reaches the RPE by P16, and progresses to the subretinal space (Supplementary Fig. 13C), where it anastomoses with the choroidal vessels at about 6 to 8 weeks of age[39]. We analyzed CD8$^+$ T cell infiltration at P18 and P50, respectively, and there was no significant change (Supplementary Fig. 13D-G). We then analyzed the expression of Sema4D on CD8$^+$ T cells by flow cytometry analysis and found that this was significantly increased in *Vldlr*$^{-/-}$ mice at both P18 and P50 (Supplementary Fig. 13H-K). We administered Conbercept, anti-Sema4D, or a combination of both at P11 and analyzed the neovascular lesions at P18. Similar to the results of the laser-induced CNV model, while Conbercept or anti-Sema4D alone had protective effects on neovascular formation, the combination treatment achieved an even better outcome in the *Vldlr*$^{-/-}$ pups (Supplementary Fig. 13L, M). In the adulthood of the *Vldlr*$^{-/-}$ mice, the abnormal vessels integrated with the choroidal vessels, creating retinal-choroidal anastomoses and choroidal neovascularization, resulting in leaky vessels detectable through FFA[39]. In mice aged 3 weeks, we administered Conbercept, anti-Sema4D, or a combination treatment. FFA analysis revealed that the combined therapy alleviated vascular leakage, displaying a significantly greater effect than Conbercept alone (Supplementary Fig. 13N, O). In conclusion, the combination of anti-angiogenic therapy and Sema4D inhibition offers substantial suppression of choroidal neovascularization, offering promise for the ongoing clinical management of nvAMD.

Discussion

AMD is characterized by the accumulation of insoluble extracellular lipid aggregates called drusen in the subretinal space during the early stage, followed by RPE and photoreceptor atrophy in the late "dry" stage, and eventually, choroid neovascularization in the late "wet" stage. Approximately 10% of patients with dry AMD progress to wet AMD, which accounts for 90% of vision loss[40]. Smoking is the most significant environmental factor and the only controllable risk factor for AMD, although its underlying mechanism remains elusive. In our study, we identified that Sema4D-PlexinB1 signaling plays a crucial role in mediating smoking-aggravated CNV via pericyte activation (Fig. 9). Targeting Sema4D-PlexinB1 through genetic and pharmacological approaches attenuated CNV and vascular leakage. Therefore, our study provides mechanistic insight into smoking-aggravated AMD and reveals the therapeutic potential of targeting the Sema4D-PlexinB1 pathway in the treatment of CNV.

In this study, we observed that smoking increased Sema4D expression on CD8$^+$ T cells, which were subsequently recruited to the CNV site, potentially due to CXCL12 produced by local cells, including pericytes. These cells activated PlexinB1 for downstream functions. Although we didn't elucidate the detailed mechanism of how Sema4D was upregulated by smoking, our data indicated that smoking increased Sema4D on CD8$^+$ T cells in peripheral white blood cells, CLN (the draining lymph nodes of the eye involved in many ocular immune diseases[41,42], and the lung, but not in other solid organs. Moreover, it is known that Sema4D is expressed in both transmembrane and secreted forms. As we didn't find a significant change in the secreted form in the serum of the mice after smoking, it seems that the effect of smoking was not mediated by the secreted forms of Sema4D.

Previous work has established that pericytes play critical roles in blood-brain barrier function, vascular development, and control of vessel contraction, blood flow, and hemostasis[25]. Although the role of pericytes in nvAMD was not completely understood, eye sections from patients with AMD reveal activated pericytes exhibiting migratory behavior near areas of macular degeneration, suggesting their involvement in the AMD disease process[43]. Another study found that choroidal-derived pericytes infiltrated the subretinal space, serving as essential cellular components that promote the deposition of ECM in the CNV mouse model[44]. In our model, using scRNA-seq, we identified three distinct populations of pericytes, each responsible for cytokine secretion, contraction, and matrix deposition, respectively. Interestingly, in both human samples and the mouse model, the number of pericytes in cluster 3, responsible for matrix deposition, was the most significantly increased population by smoking. Moreover, the cytokine secretion and fibroblast activation signatures were significantly enriched in smoke-exposed mice, implying that smoking enhances these signatures and may contribute to CNV progression. Recent studies showed that pericyte-derived "pericine" signals could directly regulate tumor cell growth as well as anti-tumor treatment sensitivity[45,46], suggesting that pericytes' cytokine production plays a significant role in disease progression. While we did not investigate whether Sema4D affects the cytokine secretion of pericytes, we observed that smoking altered the cytokine secretion signature in pericytes, suggesting that smoking may induce "pericine" signals in AMD and other disease situations, such as solid tumors.

It has been demonstrated that the activation or inhibition of downstream GTPases by Sema4D/PlexinB1 complexes depends on their interactions with specific receptor tyrosine kinases, namely ErbB2 or c-Met[47]. In cells expressing ErbB2, the binding of Sema4D to PlexinB1 activates the intrinsic tyrosine kinase activity of ErbB2, resulting in the phosphorylation of both PlexinB1 and ErbB2[33]. This, in turn, enables the activation of the ARHGEF11 and ARHGEF12, which constitutively bind to the PDZ binding site of the carboxyl-terminal

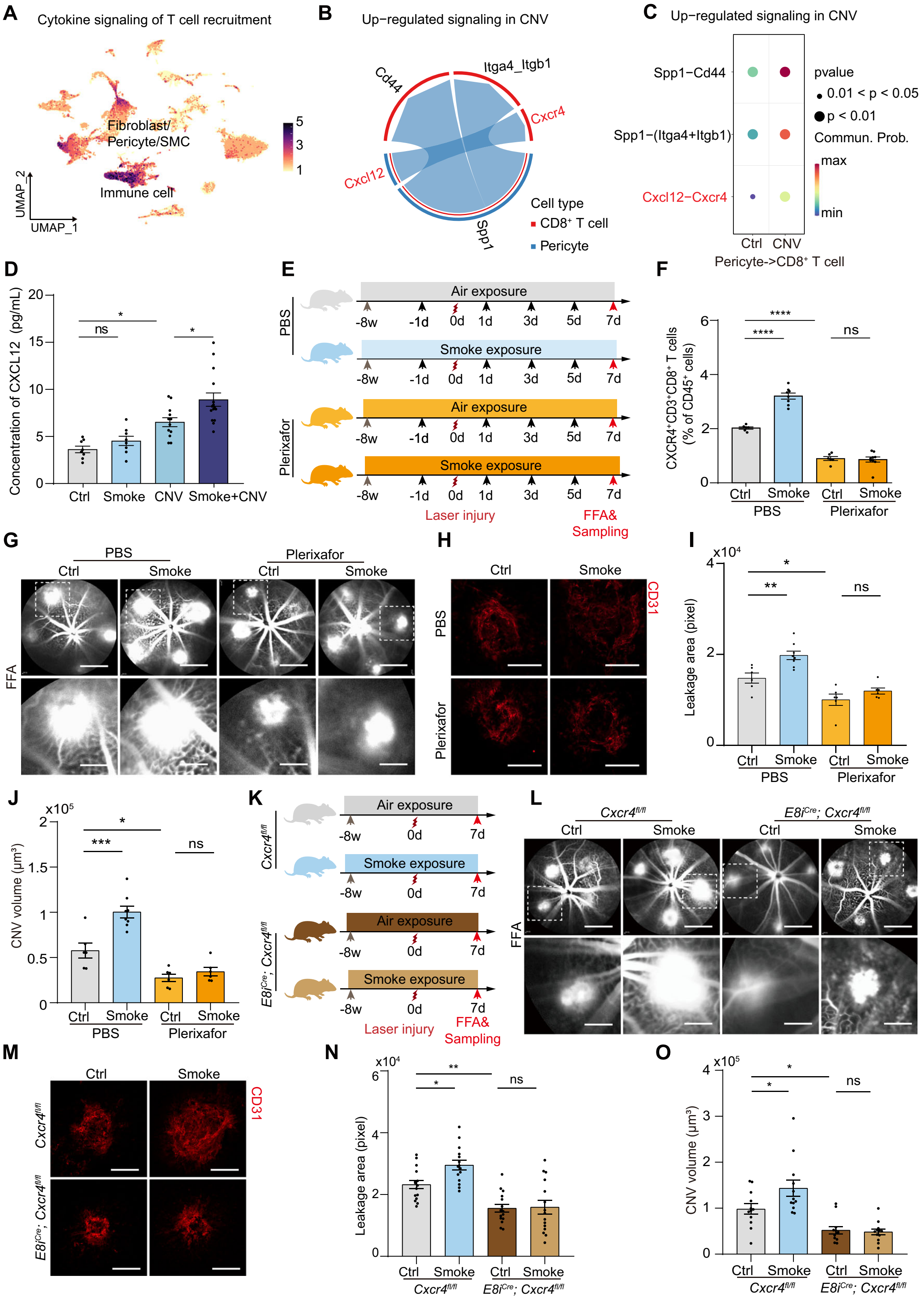

sequence of PlexinB1. The activated RhoGEFs ARHGEF11 and ARHGEF12 mediate the activation of the small GTPase RhoA, thereby stimulating various pathways. In cells lacking ErbB2 expression but containing c-Met, Sema4D/PlexinB1 recruits and activates c-Met. Phosphorylation of c-Met results in its interaction with p190 RhoGAP, leading to the inactivation of RhoA[47]. Interestingly, we observed that neither ErbB2 nor c-Met associates with PlexinB1 in pericytes. Using mass spectrometry, we identified ROR2 as an associating kinase of PlexinB1. Furthermore, we demonstrated that ROR2 is essential for the phosphorylation of PlexinB1 in pericytes, leading to the activation of the small GTPase RhoA and the stimulation of downstream pathways. Crucially, our analysis of scRNA seq data indicated that ROR2 is primarily expressed by mural cells and fibroblasts, suggesting that ROR2 may serve as a pericyte/fibroblast-specific associating kinase of

Fig. 7 | CXCL12-CXCR4 Signaling Mediates T Cell Recruitment in CNV. A UMAP illustrating the expression patterns of genes associated with cytokine signaling for T cell recruitment using scRNA-seq data from mice. **B**, **C** CellChat analysis displaying the up-regulated signaling in the CNV group compared with the Ctrl group between $CD8^+$ T cells and pericytes. **D** ELISA-measured CXCL12 concentration in vitreous fluid from Ctrl, Smoke, CNV, and Smoke + CNV groups ($n = 8/8/12/12$). Mean ± SEM, $P = 0.8047$, 0.0158, 0.0190 (one-way ANOVA, Tukey's test). **E** Schematic of smoke exposure, CNV modeling, and Plerixafor treatment. Mice received smoke exposure and Plerixafor injections, followed by CNV induction and analysis on day 7. **F** Flow cytometry analysis of $CD3^+CD8^+CXCR4^+$ cells in leukocytes ($CD45^+$) on CNV day 3 ($n = 6/8/6/9$). Mean ± SEM, $P = < 0.0001$, < 0.0001, 0.9939 (one-way ANOVA, Tukey's test). **G**, **H** Representative FFA images (**G**) and CD31-stained RPE-choroid flat mounts (**H**) on CNV day 7. Mean ± SEM, $P = < 0.0001$, < 0.0001, 0.9939 (one-way ANOVA, Tukey's test). **I**, **J** Quantification of leakage area (**I**) and CNV volume (**J**) (n = 6/8/6/6). Mean ± SEM, $P = 0.0075$, 0.0198, 0.5663, 0.0004, 0.0189, 0.8802 (one-way ANOVA, Tukey's test). **K** Schematic of smoke exposure and CNV modeling in *Cxcr4*$^{fl/fl}$ and *E8i*^{Cre}*; Cxcr4*$^{fl/fl}$ mice. **L**, **M** Representative FFA images (**L**) and CD31-stained RPE-choroid flat mounts (**M**) on day 7 after CNV modeling. **N**, **O** Quantification of leakage area (**N**) and CNV volume (**O**) ($n = 15/15/15/15$). Mean ± SEM, $P = 0.0412$, 0.0085, 0.5663, 0.0436, 0.0392, 0.9962 (one-way ANOVA, Tukey's test). $^*P < 0.05$, $^{**}P < 0.01$, $^{***}P < 0.001$, $^{****}P < 0.0001$. Scale bars: 50 μm (**H**, **M**), 80 μm (**G** lower, **L** lower), 200 μm (**G** upper, **L** upper). Source data are provided as a Source Data file.

PlexinB1. Intriguingly, although the interaction between ROR2 and semaphorin signaling has not been previously identified, ROR2 has been recognized as a Wnt receptor and may play a role in cardiovascular diseases[48]. Given existing studies suggesting a potential interaction between Wnt signaling and Sema-Plexin signaling[49], it is conceivable that ROR2 may have a role in connecting these pathways.

The CXCL12-CXCR4 axis is a well-established pathway for T cell chemotaxis[36,37]. Our cell-cell communication analysis using CellChat revealed that the pericyte-to-$CD8^+$ T cell CXCL12-CXCR4 interaction was significantly enhanced in the CNV group. Interestingly, scRNA-seq data analysis showed that CXCL12 is abundantly expressed by pericytes in both mouse and human samples. ELISA of vitreous samples from CNV and control mice exposed to either smoke or air, further confirmed that CNV increased CXCL12 levels, with smoke exposure leading to an even greater increase. Previous studies have identified multiple upstream regulators of CXCL12 production, including hypoxia, IL17A, and prostaglandin E2 (PGE2)[50–52]. During AMD pathogenesis, macular drusenopathy is associated with relative hypoxia in subretinal compartments, which contributes to the progression of AMD. Hypoxia has long been considered a critical trigger for AMD development[53]. In addition, PGE2 and IL17, important mediators of inflammation, are elevated in both CNV mouse models and AMD patients[54,55] and are further increased by smoking[56]. Although this study did not aim to identify the upstream regulatory mechanism by which CNV and smoking increase CXCL12, it is plausible that these factors might contribute to the elevation of CXCL12, thereby attracting T cells to the site of inflammation.

Although our study focused on the interaction between T cells and pericytes, it is important to note that CXCL12-CXCR4 is also known as a regulator of angiogenesis across various pathological conditions, including tumors, myocardial infarction, and ocular diseases[57–59]. In the context of CNV, previous studies have shown that CXCL12 promotes choroidal angiogenesis in mouse models[59,60]. Furthermore, in AMD patients, elevated CXCL12 levels in the vitreous fluid have been reported to correlate negatively with sensitivity to anti-VEGF treatment[61]. Therefore, it is plausible that CXCL12 produced by pericytes contributes to angiogenesis by promoting endothelial cell proliferation in CNV. In addition, as Plerixafor treatment significantly reduced vascular leakage and CNV volume in our study, it is possible that the protective effects of Plerixafor are partially mediated through inhibition of the CXCL12-CXCR4 signaling axis between pericytes and ECs.

Pathological angiogenesis is a significant characteristic of nvAMD. Standard treatments for nvAMD involve anti-angiogenic therapies targeting VEGF[40]. In addition, anti-angiogenic therapy is a primary approach in treating other vision-threatening diseases like diabetic retinopathy (DR), retinopathy of prematurity, and certain types of solid tumors. However, anti-VEGF therapy's efficacy is limited. In tumor angiogenesis, various forms of resistance to antiangiogenic therapy have been proposed[62,63]. These include the upregulation of alternative pro-angiogenic signaling pathways, recruitment of vascular progenitor cells and pro-angiogenic monocytes from the bone marrow, co-option of normal vessels or vasculogenic mimicry without necessary angiogenesis. Among these mechanisms, the protective role of pericyte coating on tumor blood vessels during anti-angiogenic therapy is considered crucial. Therefore, there is a rationale for targeting both cell types. Notably, fibrosis is also considered a significant factor in resistance to anti-angiogenic therapy[64,65]. Although this study primarily focuses on pericytes, scRNA seq data from AMD patients and mouse models indicate high levels of PlexinB1 expression in choroidal fibroblasts. Hence, it is highly probable that inhibiting Sema4D-PlexinB1 signaling could also target fibroblasts, potentially benefiting patients receiving anti-VEGF therapy.

Originally identified as axonal guidance molecules, semaphorins also regulate processes such as vascular development and angiogenesis. Sema3s, the secreted type of semaphorins in vertebrates, have been reported as anti-angiogenic factors controlling both physiological and pathological angiogenesis[66]. In the eye, Sema3C and Sema3F have been shown to inhibit retinal and subretinal angiogenesis[67,68]. DR, a leading cause of vision loss in working-age adults, exhibits abnormal retinal angiogenesis and vascular dysfunction as its main pathological characteristics. Sema3A has been found to regulate vascular permeability in DR[69], while Sema3A, Sema3E, and Sema3G have been shown to suppress revascularization during ischemic retinopathy. In addition, Sema6A has been proven to suppress reparative retinal angiogenesis[70–73]. Conversely, certain semaphorins also elicit pro-angiogenic signaling in ECs. Notably, PlexinB1 is believed to be highly expressed in ECs, and Sema4D-PlexinB1 signaling is known to promote EC migration and tube formation, driving angiogenesis in other disease conditions[66,74]. Interestingly, scRNA-seq data from both AMD patients and mouse models revealed that in the choroid, the expression level of PlexinB1 in ECs is much lower compared to pericytes. This disparity might be due to tissue- or disease-specific differences. While this study primarily focuses on CNV, it would be intriguing to explore whether PlexinB1 also plays a role in other disease conditions where pericytes are believed to be significant, such as in liver fibrosis, lung injury, and brain vascular-related diseases. Furthermore, although our study centers on vascular disorders in CNV, it is worth noting that semaphorins have been shown to play a modulatory role on T-cells[75,76], which warrants further investigation.

Semaphorins are emerging as attractive therapeutic targets. In various pathological situations, the administration of semaphorins or inhibitors of semaphorin or plexin function has demonstrated preventive or therapeutic effects in preclinical disease models. VX15/2503 (Pepinemab) is a humanized IgG4 monoclonal antibody specific to Sema4D, developed by Vaccinex. It possesses a binding affinity of about 3–5 nM and inhibits the interaction between Sema4D and PlexinB1 across several species, including humans[77]. Presently, Pepinemab has entered clinical development for patients with solid tumors (NCT01313065, NCT03268057) and neurodegenerative diseases, including early Huntington's disease and Alzheimer's disease (NCT02481674, NCT04381468), demonstrating a favorable safety profile[78–81]. Our study and its mechanistic insights suggest that AMD may also be a promising area for further clinical development

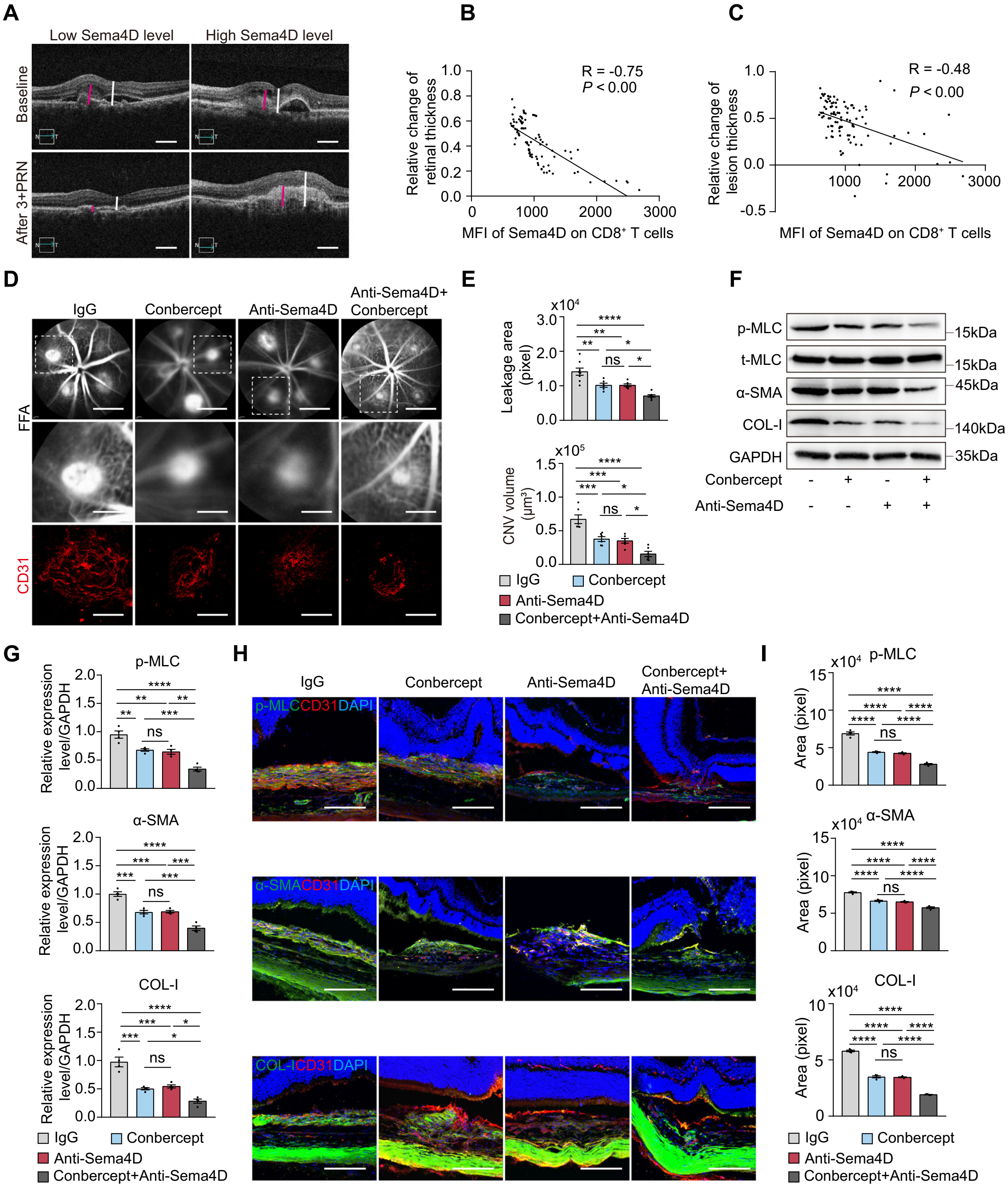

targeting Sema4D. The potential therapeutic benefits warrant further exploration in clinical settings.

While our primary focus was on nvAMD, the primary cause of vision loss, an independent study demonstrated that Sema4D can also signal to PlexinB1 expressed by RPE, leading to impaired phagocytic activity[40,82]. It has been suggested that the decline in RPE phagocytic function due to aging could contribute to drusen deposition and increased lipofuscin accumulation, ultimately resulting in RPE death and AMD. Our findings, indicating elevated Sema4D levels in mice exposed to smoke, both with or without CNV, strongly suggest that Sema4D-PlexinB1 might also play a role in the pathogenesis of AMD at an early stage.

Some limitations of this study need acknowledgment. The analysis of Sema4D expression on CD8⁺ T cells was conducted solely in peripheral blood in patients; further investigations are required to examine this signature in the eye. Moreover, as AMD is an age-related disease with age being the strongest risk factor, additional investigations should consider including elderly subjects.

In summary, by using clinical samples and animal models, we have identified a crucial role for Sema4D-PlexinB1 signaling in mediating

Fig. 8 | Targeting Sema4D alleviates CNV progression and enhances anti-VEGF therapy efficacy. A Patients with nvAMD were segregated into groups based on low and high levels of Sema4D on CD8$^+$ T cells in peripheral blood. Representative OCT images were captured at baseline and after initiating the 3 + PRN anti-VEGF treatment strategy. **B**, **C** Pearson correlation coefficient analysis was conducted between the MFI of Sema4D on CD8$^+$ T cells and changes in central retinal thickness (**B**) or lesion thickness (**C**) (normalized to baseline) in patients with nvAMD ($n = 97$). $P = < 0.0001$, < 0.0001 (Pearson correlation coefficient analysis). **D** CNV mice received intravitreal injections of IgG, Conbercept, Anti-Sema4D, or Anti-Sema4D+Conbercept. Samples were examined on CNV day 7. Representative FFA images (upper) and CD31 stained RPE-choroid-sclera flat mounts confocal images (lower) were shown. **E** Quantification of leakage area ($n = 8/6/6/7$) (upper) and CNV volume ($n = 6/6/6/6$) (lower) in (**D**). Mean ± SEM, $P = 0.0039$, 0.0038, < 0.0001, > 0.9999, 0.0328, 0.0332, 0.0009, 0.0004, < 0.0001, 0.9774, 0.0124, 0.0297 (one-way ANOVA, Tukey's test). **F**, **G** Representative blots (**F**) and quantification (**G**) of p-MLC /α-SMA/COL-I in retina-choroid complexes from mice after treatment ($n = 4/4/4/4$). Mean ± SEM, $P = 0.0042$, 0.0017, < 0.0001, 0.9524, 0.0007, 0.0017, 0.0001, 0.0002, < 0.0001, 0.9979, 0.0004, 0.0003, 0.0001, 0.0002, < 0.0001, 0.9341, 0.0384, 0.0138 (one-way ANOVA, Tukey's test). **H**, **I** Immunofluorescence staining of p-MLC/α-SMA/COL-I (green), CD31 (red), and DAPI (blue) in CNV lesion in cross-section of eyes from mice treated as indicated. Representative images (**H**) and quantification (**I**) of p-MLC, α-SMA, and COL-I-positive area are presented ($n = 4/4/4/4$). Mean ± SEM, $P = < 0.0001$, < 0.0001, < 0.0001, 0.7821, < 0.0001, < 0.0001, <0.0001, 0.6142, <0.0001, <0.0001, <0.0001, 0.9693 (one-way ANOVA, Tukey's test). * $P < 0.05$, ** $P < 0.01$, *** $P < 0.001$, **** $P < 0.0001$. Scale bars: 50 μm in (**D**, **H**), 80 mm in (**D** middle), 200 μm in (**A**, **D** upper). Source data are provided as a Source Data file.

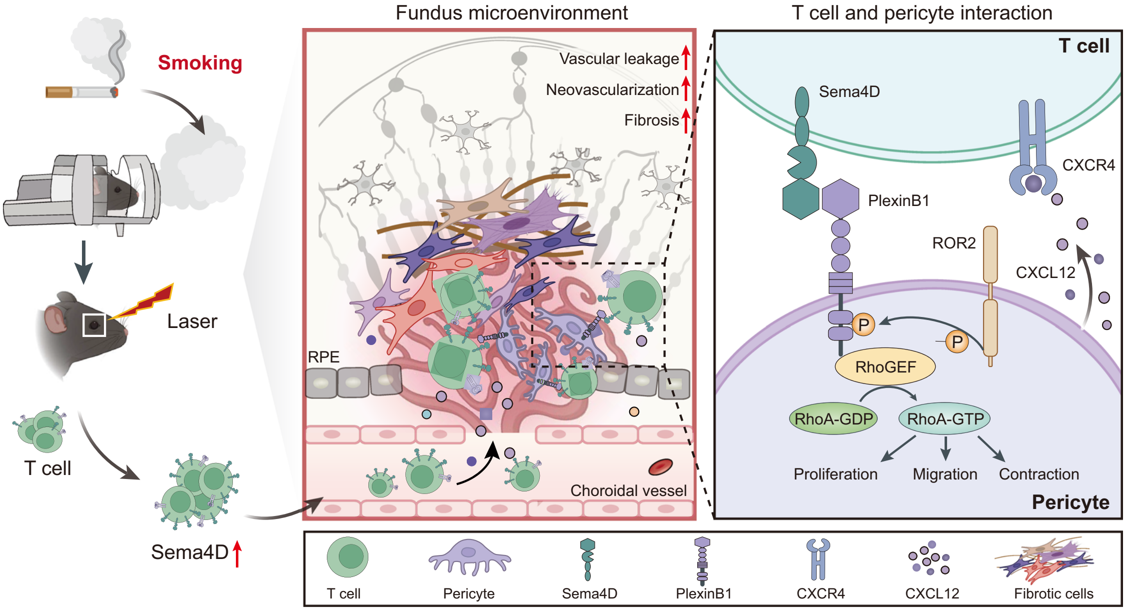

Fig. 9 | Working model. A schematic illustration presents the mechanisms. Smoking increases the expression of Sema4d in peripheral CD8$^+$ T cells, which are then recruited to the CNV lesion area via the CXCL12-CXCR4 axis. These T cells act on PlexinB1 of pericytes, activating them and thereby exacerbating CNV damage. Meanwhile, ROR2 on pericytes is a co-activating receptor for Sema4D-mediated PlexinB1 activation, promoting the phosphorylation of PlexinB1 and the activation of RhoA, which subsequently regulates pericyte proliferation, migration, and contraction.

smoking-aggravated CNV. While this finding was identified based on smoking, we also observed clear protective effects when blocking this pathway in non-smoking subjects. Thus, from a translational perspective, inhibiting the Sema4D-PlexinB1 pathway suppresses pericyte activation and reduces neovascularization in age-related macular degeneration. These insights underscore the potential therapeutic value of targeting pericytes for treating nvAMD and suggest the consideration of combination therapy with anti-VEGF treatment.

Methods

Study approval

Our study conformed to the Declaration of Helsinki. The protocol pertaining to patient sample usage was approved by the ethics committee of Tianjin Medical University General Hospital (IRB2019-WZ-101). Written informed consent were provided by donors to participate. All animal procedures were approved by the Institutional Animal Care and Use Committee of Tianjin Medical University (TMUaMEC 2020005), following the ARVO guidelines for the use of animals in vision research. The reporting of sex/gender in research and animal experiments complies with the SAGER and ARRIVE guidelines. Sex and gender are not relevant for any findings in this study and were therefore not considered in our study design, and participants was not determined based on self-report nor assigned.

Participants

Ninety-seven nvAMD patients (aged 55–88 years) were enrolled in 3 + PRN currently available anti-VEGF treatment (i.e., Conbercept, Aflibercept, or Ranibizumab) at the Department of Ophthalmology at Tianjin Medical University General Hospital. The inclusion criteria for this study included: (1) No other diseases that may affect the treatment and observation of nvAMD, such as severe cataract, diabetic retinopathy, and vascular obstruction, etc. (2). No history of treatment for wet-AMD, including anti-VEGF or laser therapy. Detailed information is presented in Supplementary Table 1. Demographic information and detailed medical histories were extracted from patient medical records, with particular attention to smoking history. Peripheral blood samples were collected during the initial patient visit and subjected to immediate flow cytometry analysis, as outlined in the "Flow Cytometry" section.

Spectral-domain OCT

Macular Cube 512 × 128 OCT scan was obtained using the same prototype device (Cirrus HD-OCT 5000, Zeiss, Germany) both at the baseline and during monthly follow-up visits. Structural parameters, specifically lesion thickness and total retinal thickness at the site of the lesion, were calculated with ImageJ software. The OCT results were analyzed by two experienced ophthalmologists.

Mice

Mice were maintained under a 12 h light-dark cycle at a temperature of 21–25 °C with a humidity level between 30 to 70% and were provided unrestricted access to food (XTI01ZJ-012, Jiangsu Synergy Pharmaceutical Biological Engineering Co., Ltd.) and water. The mice were then randomly designated into experimental groups. The mice were anesthetized with ketamine/xylazine (90 mg/10 mg per kg body weight) via intraperitoneal injection before the procedure. Adult C57BL/6 J mice were purchased from the Model Animal Research Center of Nanjing University. Cre recombinase activity was induced by intraperitoneal injection of 200 µL of Tamoxifen (Sigma, #T5648) dissolved in corn oil (20 mg/mL) for adult mice and intragastric injection of 50 µLTamoxifen (1 mg/mL) for pups at indicated time points. *Pdgfrb*^{CreERT2} (Jackson Laboratory, Stock No. 030201), *Myh11*^{CreERT2} (Jackson Laboratories, Stock No.019079) and *Sm22a*^{CreERT2} (Jackson Laboratories, Stock No.017491) mice were crossed with the *R26-tdTomato* (Jackson Laboratory, Stock No. 007914) or *R26-zsGreen* (Shanghai Model Organisms Center, Cat. NO. NM-KI-200045) for genetic lineage tracing in CNV mice model. *Pdgfrb*^{CreERT2} were crossed with *Plxnb1*$^{fl/fl}$ mice (Shanghai Model Organisms Center, Cat. NO. NM-CKO-2112373) to generate *Pdgfrb*^{CreERT2}; *Plxnb1*$^{fl/fl}$ mice and littermates genotyped as *Plxnb1*$^{fl/fl}$ were used as control group. *E8i*^{Cre} (Jackson Laboratories, Stock No. 008766) were crossed with *Cxcr4*$^{fl/fl}$ mice (Shanghai Model Organisms Center, Cat. NO. NM-CKO- NM-KO-190072) and *Sema4d*$^{fl/fl}$ mice (Cyagen Biosciences Inc, Cat. NO. S-CKO-18139) to generate CD8$^+$ T-cell-specific *Sema4d* or *Cxcr4* knockout mice, littermates genotyped as *Sema4d*$^{fl/fl}$ or *Cxcr4*$^{fl/fl}$ were used as the control group. *Sema4d*$^{-/-}$ mice (Strain NO. T014199), *Vldlr*$^{-/-}$ mice (Strain NO. T038259), and *Rag1*$^{-/-}$ (Strain NO. T004753) mice were purchased from GemPharmatech (Nanjing, China).

Smoke exposure

Male mice (8 weeks old) were subjected to nose exposure to the mainstream smoke of commercial cigarettes (Hongyun, China Tobacco, China) containing 1.2 mg of nicotine, 13 mg of CO, and 13 mg of tar oil per cigarette. This smoke exposure was generated using a smoke generator (BUXCO, NC, US), as previously described[83]. Mice were exposed for 2 h per day, five days a week, for two months. Control mice were kept in an environment with filtered air.

Electroretinogram

Electroretinogram (ERG) recordings were carried out using the Celeris D430 rodent ERG Testing system (Diagnosys LLC, MA, USA) as previous described[84]. Briefly, mice from each group were dark-adapted for more than 8 h in a light-proof dark room before recording. Mice were anaesthetized, and the pupils were dilated with one drop of 0.5% tropicamide (SINQI, China) for 5 min.

Dark adaptation was maintained throughout the recording. The Celeris apparatus has the safety light LEDs [Red (670 nm) and infrared (940 nm)] for lighting. Mice were placed on a heated platform to maintain body temperature, and corneas were kept moist with 1–2% hydroxypropyl methylcellulose (Allergan, US). Two corneal electrodes with integrated stimulators were placed on the surfaces of lubricated corneas. Impedances of ground and reference active electrodes were kept between 1.5 and 2 kΩ during recording, we kept impedances of two corneal electrodes between 2 and 5 kΩ. The stimulus intensity range (0.01, 0.1, 1 cd s/m^2) was chosen.

Laser-induced CNV Models

We used a laser-induced photocoagulation mouse model (laser-induced CNV model) in which a laser burn of Bruch's membrane triggers vessel growth from the choroid as a model for CNV[16]. Mice were anesthetized, and pupils were dilated with topical 1% tropicamide (Santen, Osaka, Japan). Four spots of laser photocoagulation (532 nm, 200 mW, 0.150 s, 100 µm; Vovus Spectra, Lumenis, US) was performed on both eyes of each mouse around the optic disk at the 3, 6, 9, and 12 o'clock positions using a slit lamp delivery system and a cover glass as a contact lens. The morphologic end-point of the laser injury was the appearance of a cavitation bubble, which correlates with the disruption of Bruch's membrane without hemorrhage. For Conbercept (anti-VEGF treatment) or/and anti-Sema4D treatment, 0.75 µg Conbercept (Chengdu Kanghong Biotechnologies Co. Ltd. China) or/and 0.75 µg anti-Sema4D (eBioscience, #BMA-12) was injected intravitreally using a 33-gauge syringe needle (Hamilton, US) in 1.5 µL volume immediately after laser burn.

Quantification of FFA and OCT

Fundus fluorescein angiography (FFA) was performed at day 7 after laser injury, using a digital fundus camera (Heidelberg Confocal Retina Angiography, Germany). Mice were anesthetized, and pupils were dilated with topical 1% tropicamide (Santen, Osaka, Japan). 100 µL of 10% fluorescein sodium (Alcon, US) were injected intraperitoneally. Fluorescent fundus images of four distinct laser burns were captured after a fluorescein circulation of 5 min. For the vascular leakage area quantification was performed as previous described[85–87]. Using ImageJ software, we delineated the high-fluorescence areas corresponding to the laser spots. For each mouse, we quantified lesions in both eyes and calculated the average value per mouse.

Mice fundus graphs and OCT images were acquired using a retinal imaging microscope (Micron IV, Phoenix Research Labs, USA). The thickness of the whole retinal layer or each sublayer were measured by the analysis software that came with the machine.

RNA Extraction and quantitative real-time PCR

Cells or tissues were harvested for RNA extraction using TRIzol reagent (#101254514, Sigma, USA). RNA concentration was determined through spectrophotometry with a Nanodrop ND-1000 (Thermo Fisher Scientific, USA). Subsequently, RNA samples were converted into complementary DNA (cDNA) using an mRNA Reverse Transcription Kit (#A301, TransGen Biotech, China) following the provided protocol instructions. Quantitative reverse transcription PCR (qRT-PCR) was conducted using SYBR™ Green Master Mix (#AQ602, TransGen Biotech, China) and the Real-Time PCR 96-well system (Applied Biosystems QuantStudio 3, USA). Primer sequences: *Plxnb1*, Forward-5′-CACACATCTACTACACTTGGCAA-3′, Reverse-5′-CAATCCCGGCTGTCATTCAC-3′; *Sema4d*, Forward-5′-CCTGGTGGTAGTGTTGAGAAC-3′, Reverse-5′-GCAAGGCCGAGTAGTTAAAGAT-3′; *Cxcr4*, Forward-5′-GAAGTGGGGTCTGGAGACTAT-3′, Reverse-5′-TTGCCGACTATGCCAGTCAAG-3′; *Il1a*, Forward-5′-CGAAGACTACAGTTCTGCCATT-3′, Reverse-5′-GACGTTTCAGAGGTTCTCAGAG-3′; *Il1b*, Forward-5′-GCAACTGTTCCTGAACTCAACT-3′, Reverse-5′-ATCTTTTGGGGTCCGTCAACT-3′; *Il6*, Forward-5′-TAGTCCTTCCTACCCCAATTTCC-3′, Reverse-5′-TTGGTCCTTAGCCACTCCTTC-3′; *Tgfb1*, Forward-5′-CTCCCGTGGCTTCTAGTGC-3′, Reverse-5′-GCCTTAGTTTGGACAGGATCTG-3′; *Tnf*, Forward-5′-CCCTCACACTCAGATCATCTTCT-3′, Reverse-5′-GCTACGACGTGGGCTACAG-3′; *Nos2*, Forward-5′-GTTCTCAGCCCAACAATACAAGA-3′, Reverse-5′-GTGGACGGGTCGATGTCAC-3′; *Gapdh*, Forward-5′-AGGTCGGTGTGAACGGATTTG-3′, Reverse-5′-TGTAGACCATGTAGTTGAGGTCA-3′. All qRT-PCR data presented in this study are the result of at least three biological replicates.

RNA Sequencing and data analyses

The retina-choroid complex was freshly dissected from mice, and RNA was extracted. Each sample was pooled of retina-choroid complexes from both eyes of one mouse. RNA quality was analyzed using an Agilent 2100 Bioanalyzer (Agilent Technologies, Santa Clara, CA, USA). Sequencing was performed at the Majorbio (Shanghai, China) on an Illumina Hiseq platform according to the manufacturer's instructions (Illumina, San Diego, CA, USA). The expression changes between groups were calculated using the DESeq2 package[88]. For gene set enrichment analysis (GSEA), gene sets were acquired from the Molecular Signatures Database (MSigDB), and GSEA_4.1.0 software was used[89–92].

Single cell RNA Sequencing

Retina-choroid complexes were harvested from mice at CNV day 3 after exposure to smoke or air for 2 months. For each group, we combined ten eyes obtained from five mice. The choroid sclera and retina were dissected and processed separately, following the established cell preparation protocol as previously described[93]. Dissociated cells from the retinas were subsequently incubated with PE anti-mouse CD73 (BioLegend, #127206, 1:300), followed by anti-PE microbeads (130-048-801, Miltenyi Biotec, US) to remove rod cells. Single-cell suspensions from both the retina and choroid-sclera were mixed and then diluted to a concentration of 200 cells/μL in a solution of 0.2% BSA/DPBS before being loaded into the 10x Genomics Chromium system. In total, this experiment included 47,053 cells, with 11,299 cells from the control group, 10,608 cells from the CNV group, 13,737 cells from the smoke-exposed group, and 11,409 cells from mice exposed to smoke and CNV.

We processed the raw data using the Cell Ranger pipeline (10 × Genomics) following the manufacturer's guidelines for analysis. Unsupervised cell clustering analysis was conducted using the Seurat 2.1 R package[94]. Cells of low quality and potential cell doublets were filtered out, including those with fewer than 200 genes, over 7500 genes, or exhibiting high mitochondrial read counts (> 20%). To mitigate batch effects, principal component analysis (PCA) was computed on the residuals for input into Harmony (version 0.1.0). We conducted uniform manifold approximation and projection (UMAP) embedding and clustering analysis on the integrated data. To identify markers for each cluster, we compiled a list of conserved cell type-specific genes using the Seurat Find Conserved Markers function. Immune cells underwent a second round of unsupervised analysis, following the same approach, utilizing the Seurat FindConservedMarkers function. We applied Gene Set Variation Analysis (GSVA) and Gene Set Enrichment Analysis (GSEA) to evaluate the changes in various gene sets among the different groups. To further investigate pericyte changes in the context of CNV and/or smoke exposure, we employed RNA velocity to identify pericyte transdifferentiation[95]. For the analysis of cell-cell communication, we used the CellChat database[96] to identify crosstalk between pericytes and $CD8^+$ T cells.

Immunofluorescence of RPE-choroid flat-mounts

Mice were sacrificed by cervical dislocation, eyes were dissected and fixed with 4% paraformaldehyde for 1 h at room temperature. The RPE-choroid complex was dissected and permeabilized with 1% Triton for 12 h and then incubated in a blocking buffer (3% BSA, 0.3% Triton PBS) at room temperature for another 12 h. Subsequently, samples were incubated with primary antibody (diluted in blocking buffer) at 4 °C for 36 h. primary antibodies used were as follows: anti-CD31 (Millipore, #MAB1398Z, 1:200); anti-RFP (Rockland, #600-401-379, 1:200); anti-CD8 (Abcam, #ab217344, 1:100); anti-α-SMA (Sigma, #A2547, 1:200); anti-PDGFRβ (Santa Cruz, #sc-374573, 1:50). After triplicate washing in 0.1% Triton PBS, the tissues were incubated with the secondary antibody (all diluted at 1:300, Goat anti-Hamster 647(Jackson, #127-605-099); Goat anti-Rabbit 594(Jackson, 111-585-003); Goat anti-Rabbit 488(Jackson, #111-545-003); Goat anti-Mouse 488(Jackson, #115-545-003)) for 2 h and mounted with neutral resin (#0100-01, SouthernBiotech, USA). Images were captured by a confocal fluorescence microscope (LSM800, Carl Zeiss, Germany). The volume of choroidal neovascularization was quantified using the surface rendering tool on Imaris software (version 9.0.1). For each mouse, we quantified lesions in both eyes and calculated the average value per mouse.

Proximity ligation assay

The experiments were conducted using the Duolink® In Situ Red Starter Kit (Sigma, #DUO92008), with RPE-choroid flat-mounts from CNV model mice. Mice were sacrificed by cervical dislocation, eyes were dissected and fixed with 4% paraformaldehyde for 1 h at room temperature. The RPE-choroid complex was dissected and permeabilized with 1% Triton for 24 h, After blocking, samples were incubated overnight at 4 °C with a mixture of anti-Sema4D (Abcam, #ab231961, 1:50), anti-PlexinB1 (Santa Cruz, #sc-28372, 1:20), and anti-CD8 (Abcam, #ab308264, 1:50) antibodies in blocking solution. Subsequently, the pre-diluted anti-rabbit plus and anti-mouse minus probes were incubated with the cells for 1 h at 37 °C. Following incubation, samples were incubated at 37 °C with ligation enzyme for 30 min and polymerase for 100 min. and the samples were incubated with the secondary antibody Goat anti-Rat 647(Jackson, #112-605-020, 1:200) before mounting and imaging.

Immunofluorescence of cross sections

The eyes were fixed in 4% paraformaldehyde at room temperature for 1 h, followed by dehydration in 30% sucrose solution for 8 h. Subsequently, they were embedded in optimal cutting temperature compound (OCT, Sakura, Japan) and snap-frozen. We then cut serial sections, each 20 μm thick, using a cryostat (CM1950, Leica, Germany), 5 slices containing CNV lesion per eye were obtained. The cross sections were brought to room temperature for 30 min, washed in PBS for 10 min, permeabilized in 0.3% Triton X-100 PBS for 15 min, and then blocked in 3% BSA, 0.3% Triton X-100 PBS for 1 h. Immunofluorescence staining with primary antibodies was carried out at 4 °C overnight, primary antibodies used were as follows: anti-CD31(Millipore, #MAB1398Z, 1:200); anti-RFP(Rockland, #600-401-379, 1:200); anti-α-SMA(Sigma, #A2547, 1:200); anti-p-MLC (Cell Signaling Technology, #3671S, 1:100); anti-COL-I (Abcam, #ab270993, 1:200)l anti-Ki67(Abcam, #ab16667, 1:200). Following washing, the sections were incubated with the corresponding secondary antibodies (all diluted at 1:300, Goat anti-Hamster 647 (Jackson, #127-605-099); Goat anti-Rabbit 594 (Jackson, #111-585-003); Goat anti-Rabbit 488 (Jackson, #111-545-003); Goat anti-Mouse 488 (Jackson, #115-545-003)) for 2 h at room temperature. Image acquisition was performed using a confocal fluorescence microscope (LSM800, Carl Zeiss, Germany). For each set of experiments, the same settings were used for collecting confocal images. The images were quantified by ImageJ software. Three images from each tissue were used for analysis.

Fluorescence-activated cell sorting

To isolate $CD8^+$ T cells, spleens of the mice (*Sema4d*$^{-/-}$ or *Sema4d*$^{+/+}$, *E8i*^{Cre}*; Sema4d*$^{fl/fl}$ or *Sema4d*$^{fl/fl}$, *E8i*^{Cre}*; Cxcr4*$^{fl/fl}$ or *Cxcr4*$^{fl/fl}$) were removed immediately after scarified, ground gently in a 40 μm strainer, and stained for cell surface antigen after lysis of post-red blood cells by ACK Lysis Solution (R1010, Solaribio, China). Antibodies were as follows: FITC anti-mouse CD45 (BioLegend, #103108, 1:300); APC anti-mouse CD3 (BioLegend, #100236, 1:300); PerCP/Cyanine5.5 anti-mouse CD8 (BioLegend, #100734, 1:300).

To confirm the effectiveness of *Plxnb1* deletion in *Plxnb1*^{CreERT2} *Pdgfrb*$^{fl/fl}$ mice, we isolated pericytes from the mouse brain. The brain samples were dissected and disassociated (in 1640 basic medium containing 0.25 mg/mL DNase I, 3 mg/mL collagenase/Dispase) for 10 min at 37 °C. For myelin depletion, we employed a magnetic cell separation method involving myelin depletion magnetic beads from Miltenyi Biotec. Pericytes sorting ($CD31^-CD140b^+$) was performed using FACS Aria Fusion (BD Biosciences, US). Antibodies were as follows: FITC anti-mouse CD31 (BioLegend, #102405, 1:300); APC anti-mouse CD140b (BioLegend, #136008, 1:300).

Cell transfusion

CD8$^+$ T cells were sorted from *Sema4d*$^{+/+}$ or *Sema4d*$^{-/-}$ mice by FACS as described above. After centrifuged, cells were resuspended in normal saline for 1×10^7 cells/mL, and each *Rag*$^{-/-}$ mouse received 100 μL cell suspension (1×10^6 cells) through tail vein injection, or 100 μL saline. At the same time, a laser-induced CNV model was established, and the success of blood transfusion was verified by a frozen section for eyeball on day 3 of CNV. FFA and choroid flat-mounts on day 7 after CNV modeling were used to compare the effect of blood transfusion.

Flow cytometry

For flow cytometry analysis of the peripheral blood samples from nvAMD patients or mice, blood samples were collected in anticoagulant tubes containing heparin sodium. Subsequently, the blood samples were centrifuged at 4 °C for 10 min at 3000 rpm using la ymphocyte separation medium. Afterward, we selectively lysed the erythrocytes by applying ACK lysis solution (#R1010, Solaribio, China). The resulting peripheral blood mononuclear cells (PBMCs) were stained with labeled antibodies on ice for 30 min before flow cytometry analysis.

For flow cytometry analysis of the spleen samples, the spleens of the mice were promptly removed upon sacrifice and were gently ground through a 100 μm strainer and subjected to cell surface antigen staining following the lysis of red blood cells using ACK Lysis Solution. For the eye, CLN, and lung samples, the tissues were collected immediately after sacrifice and were minced into small pieces using micro scissors. The tissue fragments were then incubated in a digest buffer (comprising 1640 basic medium with 0.25 mg/mL DNase I and 3 mg/mL collagenase/Dispase) for 10 min at 37 °C. Single cells were isolated using a 40 μm strainer, and the digestion process was terminated by introducing 5% BSA. The antibodies were as followed:

PerCP/Cyanine5.5 anti-mouse CD45 (BioLegend, #103131, 1:300); FITC anti-mouse CD45 (BioLegend, #103108, 1:300); APC anti-mouse CD3 (BioLegend, #100236, 1:300); APC/Cyanine7 anti-mouse CD3 (BioLegend, #100221, 1:300); PerCP/Cyanine5.5 anti-mouse CD8 (BioLegend, #100734, 1:300); PE/Cyanine7 anti-mouse CD4 (BioLegend, #100422, 1:300); FITC anti-mouse NK1.1 (BioLegend, #156508, 1:300); APC anti-mouse CD19 (BioLegend, #115512, 1:300); PerCP/Cyanine5.5 anti-mouse CD11b (BioLegend, #101228, 1:300); PE-Cyanine7 anti-mouse F4/80 (BioLegend, #123114, 1:300); APC/Cyanine7 anti-mouse Ly6G (BioLegend, #127624, 1:300); PE anti-mouse Sema4D (BioLegend, #147603, 1:300); PE anti-mouse CXCR4 (BioLegend, #146505, 1:300); anti-PlexinB1 (Santa Cruz, #sc-28372, 1:100); PE Goat anti-mouse IgG (BioLegend, #405307, 1:300); FITC anti-mouse CD31(BioLegend, #102405, 1:300); APC anti-mouse CD140b (BioLegend, #136008, 1:300); APC/Cyanine7 anti-human CD45 (BioLegend, #304014, 1:300); APC anti-human CD3 (BioLegend, #317317, 1:300); FITC anti-human CD4 (BioLegend, #344604, 1:300); PerCP anti-human CD8 (BioLegend, #344708, 1:300); FITC anti-human CD19 (BioLegend, #302206, 1:300); PE anti-human Sema4D (BioLegend, #328407, 1:300).

Cells were washed twice and analysis were performed using a FACSVerse flow cytometer (BD Biosciences, US), and the FlowJo (Version 10) software.

Cell culture

Human brain vessel pericyte cells (HBVPC) were obtained from Sciencell (#1200, US) and cultured in a pericyte medium (PM, #1201, Sciencell, US). For HBVPCs wound closure assays, confluent cells were starved in a medium without FBS overnight. Linear scratch wounds were gently created using a sterile 200 μl pipette tip. Subsequently, the cells were treated with Sema4D (1.6 μg/mL) (#CD0-H5257, ACROBiosystems, China) in PM with 2% FBS and 1% pericyte growth factor for an additional 8 h. The progress of wound closure was observed at specified time points using a microscope equipped with a digital camera. ImageJ software was employed to analyze the wound area. For the collagen gel contraction assay, the procedure followed the previous descriptions[65]. In summary, the gel mixture was prepared with collagen type I (#354249, Corning, US) and Matrigel (#354230, Corning, US). A 100 μL mixture of cells and gel was placed in a 96-well plate, with final concentrations of 2.5×10^5 MBVPCs cells/mL, 4 mg/mL collagen, and 2 mg/mL Matrigel, respectively. After the gel polymerized, the culture was incubated with 200 μL of fresh media containing different treatments. Gel contraction was observed at specific time points using a stereomicroscope (Leica M12, Germany), and the images were analyzed using ImageJ software. For ROR2 and RhoA inhibition experiments, we treated HBVPCs at a density of 90% with Sema4D (1.6ug/mL) for 8 h in the presence or absence of anti-ROR2 (MedChemExpress, #HY-145626) (1 μg/mL) or the RhoA inhibitor Rhosin hydrochloride (MedChemExpress, #HY-12646) (40 μM). After the treatment, the cells were harvested for further analysis.

Mouse brain vessel pericyte cells (MBVPCs) were obtained from Procell (#CP-M194, Procell, China) and cultured in pericyte medium (#CM-M194, Procell, China). For the CD8$^+$ T cell and MBVPC co-culture assay, CD8$^+$ T cells were isolated from the spleens of *C57BL/6 J*, *Sema4d* $^{-/-}$ or *Sema4d* $^{+/+}$ mice through fluorescence-activated cell sorting (FACS). 1×10^6 CD8$^+$ T cells were co-cultured with pre-starved MBVPCs or siRNA transfected MBVPC per well in a 6-well plate. Gel contraction analysis, wound closure assays, and immunoblotting were conducted after 48 h of co-culture.

siRNA transfection

Sixteen hours prior to transfection, cells were seeded in a six-well plate and allowed to reach 70 to 80% confluency. Transfection was performed using Lipofectamine™ RNAiMAX (#13778150, Invitrogen, US) and either control siRNA (siCtrl) or siRNA targeting HBVPC *PLXNB1* or *ROR2*, and MBVPC *Plxnb1*, following the manufacturer's instructions. The siRNA solution was used at a final concentration of 160 nM. The sequences of siRNA for HBVPCs: si*PLXNB1*, 5′-ACCACGGU-CACCCGGAUUCTT-3′. si*ROR2*, 5′-TACGTCACACAGTTCCACT-3′. The sequences of siRNA for MBVPCs: si*Plxnb1*, 5′- AATTCATGGAA-CATGAATGGC-3′.

Immunoprecipitation and immunoblotting

Coimmunoprecipitation assays were performed as previously described[97]. Cells were lysed using mild lysis buffer [20 mM tris at pH 7.5, 150 mM NaCl, 5 mM EDTA, 1% NP-40, 10% glycerol, 1 × protease inhibitor cocktail, and 1 × phosphatase inhibitor (Roche)]. Cell lysates were centrifuged for 10 min, and supernatants were used for immunoprecipitation. To immunoprecipitate Flag-tagged proteins, supernatants were collected and incubated with anti-Flag M2 magnetic beads (Sigma-Aldrich, #M8823). The beads were washed, and 3 × Flag peptide was applied to elute the Flag-protein complex. The antibodies used for immunoblotting were as follow: anti-p-MLC (Cell Signaling Technology, #3671S,1:2000); anti-t-MLC (Cell Signaling Technology, #2672S, 1:2000); anti-α-SMA (Sigma, #A2547, 1:2000); anti-Collagen-I (Abcam, #ab34710,1:2000); anti-Collagen-I (Abcam, # ab270993,1:2000); anti-Flag (Sigma, #A8592-0.2MG, 1:4000); anti-ROR2 (Santa Cruze, #sc-374174, 1:500); anti-RhoA (Santa Cruze, #sc-418, 1:1000); anti-c-MET (Cell Signaling Technology, #8198 T, 1:2000); anti-ErbB2 (Cell Signaling Technology, #4290 T, 1:2000); 1:3000; anti-PlexinB1 (Santa Cruze, #sc-28372, 1:500); anti-p-Tyr (Millipore, #05-321, 1:1000); anti-GAPGH (ABclonal, #AC033, 1:5000); Peroxidase AffiniPure Goat anti-Mouse IgG (H + L) (Jackson, #115-035-003,1:3000); Peroxidase AffiniPure Goat anti-Rabbit IgG (H + L) (Jackson, #111-035-003, 1:3000). All the uncropped scans of the blots are provided in the Source Data file.

Choroid sprouting assay

The choroid explant sprouting assay was performed as the previously described[17]. Briefly, the choroid- RPE complex was dissected and cut into 1 mm × 1 mm pieces, followed by incubation in M199 medium (containing 1% Penicillin and streptomycin, 10% FBS, 1% endothelial cell growth factor) for a duration of 6 h. Subsequently, the choroid explants were embedded into Matrigel (354230, Corning, US) and cultured in M199 medium for 48 h. Afterward, the explants were treated with 1.6 μg/mL of mouse Sema4D (R&D, #5235-S4B) for another 48 h, while the control group received IgG protein (R&D, # MAB002). The sprouting choroidal explants were then fixed using 4% paraformaldehyde, stained with phalloidin, and subjected to imaging with a confocal fluorescence microscope (LSM800, Carl Zeiss, Germany). The sprouting area and vessel length were quantified through the utilization of ImageJ software.

ELISA Analysis

Vitreous humor samples were collected from the vitreous cavity using a 31 G insulin syringe. ELISA tests for the detection of mouse CXLC12 (ml063391-1, Shanghai Enzyme-linked Biotechnology Co., Ltd., China) and soluble Sema4D (YK-E2675, Shanghai Yukang Electromechanical Equipment Co., Ltd., China) were performed following the manufacturer's instructions.

TUNEL Assay

TUNEL assays were conducted using a one-step TUNEL Apoptosis Assay Kit (C1088, Beyotime, China), following the instructions provided by the manufacturer. In brief, cryosections were brought to room temperature, washed in PBS for 10 minutes, and subsequently incubated in 3% BSA, 0.3% Triton X-100 PBS for 5 min. Nuclei were labeled with DAPI. To count the TUNEL-positive cells, the sections were mounted with neutral resin, and images were captured using a confocal laser scanning microscope (LSM 800; ZEISS, Germany).

Adenoviral production

The DNA fragment of Plexin-B1 (Ensembl: ENSG00000164050) were obtained from Addgene (Addgene_70469). AdC68-Flag-PlexinB1 were generated as previously described[98], HEK 293 A cell line (ATCC CRL-1573) was used for the package the adenovirus. HBVPCs were infected with adenovirus at the multiplicity of infection of ~ 100. Cells were used for analysis 36 h after infection.

Mass spectrometry analysis

Trypsin digestion. HBVPCs were infected with AdC68-Flag-PlexinB1 and then subjected to Sema4D stimulation. Anti-FLAG M2 Magnetic Beads (Sigma-Aldrich, St. Louis, MO), were utilized to capture the FLAG protein complex in the cell lysates. Following binding, the magnetic beads underwent washing with cold PBS plus 0.1% NP-40. The elution of the FLAG-protein complex was conducted using a FLAG peptide. After gel electrophoresis, gel bands were cut into small pieces (1 mm). These gel pieces were destained with 25 mM ammonium bicarbonate in ethanol/water (1:1, v/v). Then, the destained gel pieces were rinsed in an acidic buffer (acetic acid/ethanol/water, 1:5:4, v/v/v) two times, each for 1 hour, and twice in water, each for 10 min. Afterward, the gel pieces were dehydrated in acetonitrile and dried in a SpeedVac (Thermo Fisher). Disulfide bonds were cleaved using dithiothreitol (10 mM) at 56 °C for 1 h and the cleaved bonds were protected by Iodoacetamide (55 mM) at room temperature for 45 minutes. After two water washes, the gel pieces were dehydrated in acetonitrile and dried in a SpeedVac (Thermo Fisher). Subsequently, 200 nanograms of trypsin (Promega), dissolved in 50 mM ammonium bicarbonate, was added to the dried gels and incubated overnight at 37 °C. Tryptic peptides were then extracted sequentially from the gel pieces using 50% acetonitrile (acetonitrile/water/TFA, 50:45:5, v/v/v), 75% acetonitrile (acetonitrile/water/TFA, 75:25:0.1, v/v/v), and acetonitrile. The peptide extracts were pooled, dried in a SpeedVac, and desalted using a μ-C18 Ziptip.

MS/MS Analysis. The digested sample was injected into a Nano-LC system (EASY-nLC 1200, Thermo Fisher Scientific). Each sample was separated by a C18 column (75 μm inner diameter × 25 cm, 3 μm C18) at a flow rate of 300 nL/min. The HPLC gradient was as follows: 5% to 10% solvent B (0.1% formic acid in 80% acetonitrile) in 16 min, 10% to 22% solvent B in 35 min, 22% to 30% solvent B in 15 min, 30% to 90% solvent B in 1 min, and holding for 8 min at 90% solvent B. The HPLC eluate was electrospray directly into an Orbitrap Eclipse mass spectrometer (Thermo Fisher Scientific). The source operated at 2.2 kV. The mass spectrometric analysis was performed in a data-dependent mode. For the MS1 survey scan, the automatic gain control (AGC) target was set to 5e4, and the resolution was 70,000. The MS2 spectra were acquired with a resolution of 17,500.

Data processing. The resulting MS/MS data were processed using Proteome Discoverer 3.0 with an overall false discovery rate (FDR) for peptides of less than 1%. Trypsin (Full) was specified as the cleavage enzyme, allowing up to two missing cleavages. The mass tolerance for precursor ions was set to 10 ppm in the first search, and the mass tolerance for fragment ions was set to 0.02 Da. Carbamidomethyl on Cys was designated as a fixed modification, and Met acetylation and oxidation were designated as variable modifications. Mass tolerances for precursor ions were set at ±10 ppm for precursor ions and ± 0.02 Da for MS/MS.

RhoA activation assay

RhoA activity in HBVPCs or MBVPCs was detected by G-LISA (BK124-S, Cytoskeleton, US) according to the manufacturer's instructions. To examine the effect of PlexinB1 and ROR2, cells were transfected with si*PLXNB1*, si*ROR2,* or control siRNA for 48 h before Sema4D stimulation. For the co-culture of CD8$^+$ T cells and MBVPCs, CD8$^+$ T cells were sorted from *Sema4d*$^{-/-}$ or *Sema4d*$^{+/+}$ mice through FACS. 1 × 10^6 CD8$^+$ T cells were co-cultured with pre-starved MBVPCs per well in a 6-well plate. RhoA activation assay were conducted after 48 h of co-culture.

Microfluidic chip assay

Microfluidic chip assay was performed as previously described[99,100]. In summary, HUVECs (labeled with lenti-mCherry) and HBVPCs (labeled with lenti-EGFP, and transfected with siCtrl or si*PLXNB1*) were trypsinized and suspended in a mixture containing 5 mg/mL fibrinogen (Sigma, #F8630) with 0.15 U/mL aprotinin (Sigma, #A1153-25 MG) at a density of 8 × 10^6 cells/mL for HUVECs and 8 × 10^5 cells/mL for HBVPCs. The cell suspension was combined with 1 U/mL thrombin (Sigma, #T4648-1KU) before being injected into the microfluidic channel. After the gel had polymerized, the chips were placed in a humid chamber and received fresh EBM-2 (#CC-3156, LONZA), every 2 days. Sema4D (1.6 μg/mL) was introduced into the medium for an additional 2 days on day 4. On day 10, the cells were fixed by adding 4% paraformaldehyde to the medium channel for 6 h. Images were captured by a confocal fluorescence microscope (Andor Dragonfly, UK). The images were processed by Imaris v9.0.1 software.

To perform the fluidic-based leakage assay, the chips were positioned on an inverted microscope equipped with a humid CO$_2$ culturing thermo chamber. The medium in the channel was aspirated, and 0.01% 100 nm FITC-conjugated microbeads (Hugebio, #GF100C) were added into one end of the channel, allowing them to flow into the vessel due to the difference in height. Images were taken at 3-minute intervals by a confocal fluorescence microscope (Andor Dragonfly, UK). Leakage assessment was carried out using Image J by analyzing the fluorescence intensity from the lumen side of the vessel wall to the ECM side. Fluorescence intensity was standardized within each measurement. The ratio of fluorescence intensity between the ECM and the vessel lumen was employed for subsequent statistical analysis.

Statistical analysis

All experiment statistical analyses were performed using GraphPad Prism 8.0.1 software (GraphPad Software, San Diego, CA). Results are presented as the mean ± SEM of biological replicates. Statistical methods for comparison of experimental groups in each experiment are indicated in the figure legends. To calculate the statistical significance of differences between the two groups, a two-tailed unpaired Student's t test was used. One-way analysis of variance (ANOVA) followed by Tukey's multiple comparisons was used to determine the statistical significances three or more groups. Two-way ANOVA was used to compare the relative lesion recovery in patients with nvAMD and body weight change of smoking mice. Pearson's chi-square test is used to detect differences in the incidence of AMD-related complications between the two groups of patients. Pearson correlation coefficient analysis was performed to examine the relationships between the MFI of Sema4D on CD8$^+$ T cells and the lesion recovery rate in patients. A value of $P < 0.05$ was considered significant. * $P < 0.05$, ** $P < 0.01$, *** $P < 0.001$, **** $P < 0.0001$. The sample size was determined according to a previous publication where at least three animals per group were analyzed[101]. Mice were randomly assigned for different treatments. No animals were excluded from the study. All experimenters were blinded both during the execution and analysis of experiments.

Reporting summary

Further information on research design is available in the Nature Portfolio Reporting Summary linked to this article.

Data availability

The RNA-seq data generated in this study have been deposited in the Gene Expression Omnibus (GEO) database under accession code GSE288035 for bulk RNA-seq and GSE288036 for scRNA seq. The mass spectrometry proteomics data have been deposited to the ProteomeXchange Consortium via the PRIDE72 partner repository with the dataset identifier PXD059165. The remaining data are available within the Article, Supplementary Information, or Source Data file. Source data are provided in this paper.

References

1. Wong, W. L. et al. Global prevalence of age-related macular degeneration and disease burden projection for 2020 and 2040: a systematic review and meta-analysis. *Lancet Glob. Health* **2**, E106–E116 (2014).
2. Rein, D. B. et al. Forecasting age-related macular degeneration through the year 2050 the potential impact of new treatments. *Arch. Ophthalmol.* **127**, 533–540 (2009).
3. Coleman, H. R., Chan, C. C., Ferris, F. L. 3rd & Chew, E. Y. Age-related macular degeneration. *Lancet* **372**, 1835–1845 (2008).
4. Clemons, T. E., Milton, R. C., Klein, R., Seddon, J. M. & Ferris, F. L. 3rd Risk factors for the incidence of advanced age-related macular degeneration in the age-related eye disease study (AREDS) AREDS report no. 19. *Ophthalmology* **112**, 533–539 (2005).
5. Yang, S. et al. Targeting C3b/C4b and VEGF with a bispecific fusion protein optimized for neovascular age-related macular degeneration therapy. *Sci. Transl. Med.* **14**, eabj2177 (2022).
6. Mettu P. S., Allingham M. J., Cousins S. W. Incomplete response to Anti-VEGF therapy in neovascular AMD: Exploring disease mechanisms and therapeutic opportunities. *Prog. Retin. Eye Res.* **82**, https://doi.org/10.1016/j.preteyeres.2020.100906 (2021).
7. Menger, J. F., Haubitz, I. & Keilhauer-Strachwitz, C. N. Influence Of AMD-Risk factors on the effectiveness of anti-VEGF therapy in neovascular age-related macular degeneration. *Invest. Ophthalmol. Vis. Sci.* **53**, 857–857 (2012).
8. van Splunder, H., Villacampa, P., Martínez-Romero, A. & Graupera, M. Pericytes in the disease spotlight. *Trends Cell Biol.* **34**, 58–71 (2024).
9. Armulik, A. et al. Pericytes regulate the blood-brain barrier. *Nature* **468**, 557–561 (2010).
10. Morikawa, S. et al. Abnormalities in pericytes on blood vessels and endothelial sprouts in tumors. *Am. J. Pathol.* **160**, 985–1000 (2002).
11. van Splunder H., Villacampa P., Martinez-Romero A., Graupera M. Pericytes in the disease spotlight. *Trends Cell Biol.* **34**, 58–71 (2023).
12. Benjamin, L. E., Golijanin, D., Itin, A., Pode, D. & Keshet, E. Selective ablation of immature blood vessels in established human tumors follows vascular endothelial growth factor withdrawal. *J. Clin. Invest.* **103**, 159–165 (1999).
13. Roth, L. et al. The many faces of semaphorins: from development to pathology. *Cell. Mol. Life Sci.* **66**, 649–666 (2009).
14. Worzfeld, T. & Offermanns, S. Semaphorins and plexins as therapeutic targets. *Nat. Rev. Drug Discov.* **13**, 603–621 (2014).
15. Elhabazi, A., Delaire, S., Bensussan, A., Boumsell, L. & Bismuth, G. Biological activity of soluble CD100. I. The extracellular region of CD100 is released from the surface of T lymphocytes by regulated proteolysis. *J. Immunol.* **166**, 4341–4347 (2001).
16. Lambert, V. et al. Laser-induced choroidal neovascularization model to study age-related macular degeneration in mice. *Nat. Protocols* **8**, 2197–2211 (2013).
17. Tomita, Y. et al. An ex vivo choroid sprouting assay of ocular microvascular angiogenesis. *J. Vis. Exp.* **162**, https://doi.org/10.3791/61677 (2020).
18. Voigt, A. P. et al. Single-cell transcriptomics of the human retinal pigment epithelium and choroid in health and macular degeneration. *Proc. Natl. Acad. Sci. USA* **116**, 24100–24107 (2019).
19. Hall, K. T. et al. Human CD100, a novel leukocyte semaphorin that promotes B-cell aggregation and differentiation. *Proc. Natl. Acad. Sci. USA* **93**, 11780–11785 (1996).
20. Dong, X. et al. Natural killer cells promote neutrophil extracellular traps and restrain macular degeneration in mice. *Sci. Transl. Med.* **16**, eadi6626 (2024).
21. Suzuki, K., Kumanogoh, A. & Kikutani, H. Semaphorins and their receptors in immune cell interactions. *Nat. Immunol.* **9**, 17–23 (2008).
22. López-Cano, M., Fernández-Dueñas, V. & Ciruela, F. Proximity ligation assay image analysis protocol: Addressing receptor-receptor interactions. *Methods Mol. Biol.* **2040**, 41–50 (2019).
23. Brash, J. T. et al. Tamoxifen-activated CreERT impairs retinal angiogenesis independently of gene deletion. *Circ. Res.* **127**, 849–850 (2020).
24. Rashbrook, V. S., Brash, J. T. & Ruhrberg, C. Cre toxicity in mouse models of cardiovascular physiology and disease. *Nat. Cardiovasc. Res.* **1**, 806–816 (2022).
25. Armulik, A., Genové, G. & Betsholtz, C. Pericytes: developmental, physiological, and pathological perspectives, problems, and promises. *Dev. Cell* **21**, 193–215 (2011).
26. Zhang, Q. et al. Collagen gel contraction assays: From modelling wound healing to quantifying cellular interactions with three-dimensional extracellular matrices. *Eur. J. Cell Biol.* **101**, 151253 (2022).
27. Gaengel, K., Genové, G., Armulik, A. & Betsholtz, C. Endothelial-mural cell signaling in vascular development and angiogenesis. *Arterioscler. Thromb. Vas. Biol.* **29**, 630–638 (2009).
28. Meng, Y. M. et al. Hexokinase 2-driven glycolysis in pericytes activates their contractility leading to tumor blood vessel abnormalities. *Nat. Commun.* **12**, 6011 (2021).

29. Chen, M. B. et al. On-chip human microvasculature assay for visualization and quantification of tumor cell extravasation dynamics. *Nat. Protocols* **12**, 865–880 (2017).
30. Aurandt, J., Vikis, H. G., Gutkind, J. S., Ahn, N. & Guan, K. L. The semaphorin receptor plexin-B1 signals through a direct interaction with the Rho-specific nucleotide exchange factor, LARG. *Proc. Natl. Acad. Sci. USA*. **99**, 12085–12090 (2002).
31. Driessens, M. H., Olivo, C., Nagata, K., Inagaki, M. & Collard, J. G. B plexins activate Rho through PDZ-RhoGEF. *FEBS Lett.* **529**, 168–172 (2002).
32. Hirotani, M. et al. Interaction of plexin-B1 with PDZ domain-containing Rho guanine nucleotide exchange factors. *Biochem. Biophys. Res. Commun.* **297**, 32–37 (2002).
33. Swiercz, J. M., Kuner, R. & Offermanns, S. Plexin-B1/RhoGEF-mediated RhoA activation involves the receptor tyrosine kinase ErbB-2. *J. Cell Biol.* **165**, 869–880 (2004).
34. Giordano, S. et al. The semaphorin 4D receptor controls invasive growth by coupling with Met. *Nat. Cell Biol.* **4**, 720–724 (2002).
35. Negishi-Koga, T. et al. Suppression of bone formation by osteoclastic expression of semaphorin 4D. *Nat. Med.* **17**, 1473–1480 (2011).
36. Bleul, C. C., Fuhlbrigge, R. C., Casasnovas, J. M., Aiuti, A. & Springer, T. A. A highly efficacious lymphocyte chemoattractant, stromal cell-derived factor 1 (SDF-1). *J. Exp. Med.* **184**, 1101–1109 (1996).
37. Zou, Y. R., Kottmann, A. H., Kuroda, M., Taniuchi, I. & Littman, D. R. Function of the chemokine receptor CXCR4 in haematopoiesis and in cerebellar development. *Nature* **393**, 595–599 (1998).
38. Ma, Q. et al. CXCR4 blockade in macrophage promotes angiogenesis in ischemic hindlimb by modulating autophagy. *J. Mol. Cell.Cardiol.* **169**, 57–70 (2022).
39. Sun, Y. et al. Inflammatory signals from photoreceptor modulate pathological retinal angiogenesis via c-Fos. *J. Exp. Med.* **214**, 1753–1767 (2017).
40. Apte, R. S. Reducing treatment burden in AMD. *Cell* **180**, 1033 (2020).
41. Nakao, S. et al. Lack of lymphatics and lymph node-mediated immunity in choroidal neovascularization. *Invest. Ophthalmol. Vis. Sci.* **54**, 3830–3836 (2013).
42. Bian, J. et al. Targeting NF-κB c-Rel in regulatory T cells to treat corneal transplantation rejection. *Am. J. Transplant.* **21**, 3858–3870 (2021).
43. Sarks, J. P., Sarks, S. H. & Killingsworth, M. C. Morphology of early choroidal neovascularisation in age-related macular degeneration: correlation with activity. *Eye* **11**, 515–522 (1997).
44. Luo, X. et al. Choroidal pericytes promote subretinal fibrosis after experimental photocoagulation. *Dis. Model Mech.* **11**, https://doi.org/10.1242/dmm.032060 (2018).
45. Wong, P. P. et al. Cancer burden is controlled by mural cell-beta3-integrin regulated Crosstalk with Tumor Cells. *Cell* **181**, 1346–1363 (2020).
46. Huang, C. et al. Pericytes modulate third-generation tyrosine kinase inhibitor sensitivity in EGFR-mutated lung cancer cells through IL32-β5-integrin paracrine signaling. *Adv. Sci.* 11, e2405130 (2024).
47. Swiercz, J. M., Worzfeld, T. & Offermanns, S. ErbB-2 and met reciprocally regulate cellular signaling via plexin-B1. *J. Biol. Chem.* **283**, 1893–1901 (2008).
48. Akoumianakis, I., Polkinghorne, M. & Antoniades, C. Non-canonical WNT signalling in cardiovascular disease: mechanisms and therapeutic implications. *Nat. Rev. Cardiol.* 783–797 (2022).
49. Cheng, S. & Özkan, E. Finally on track: Interactions of off-track with plex-sema pathway and glycosaminoglycans. *Structure* **28**, 492–494 (2020).
50. Strickland, J., Garrison, D. & Copple, B. L. Hypoxia upregulates Cxcl12 in hepatocytes by a complex mechanism involving hypoxia-inducible factors and transforming growth factor-β. *Cytokine* **127**, 154986 (2020).
51. Chang, Y. H. et al. Protective role of IL-17-producing γδ T cells in a laser-induced choroidal neovascularization mouse model. *J. Neuroinflammation* **20**, 279 (2023).
52. Obermajer, N., Muthuswamy, R., Odunsi, K., Edwards, R. P. & Kalinski, P. PGE(2)-induced CXCL12 production and CXCR4 expression controls the accumulation of human MDSCs in ovarian cancer environment. *Cancer Res.* **71**, 7463–7470 (2011).
53. Vadlapatla, R. K., Vadlapudi, A. D. & Mitra, A. K. Hypoxia-inducible factor-1 (HIF-1): a potential target for intervention in ocular neovascular diseases. *Curr. Drug Targets* **14**, 919–935 (2013).
54. Zhan, P. et al. PGE(2) promotes macrophage recruitment and neovascularization in murine wet-type AMD models. *Cell Commun. Signal.* **20**, 155 (2022).
55. Chen, J., Wang, W. & Li, Q. Increased Th1/Th17 responses contribute to low-grade inflammation in age-related macular degeneration. *Cellular Physiol. Biochem.* **44**, 357–367 (2017).
56. Huang, R. Y. & Chen, G. G. Cigarette smoking, cyclooxygenase-2 pathway and cancer. *Biochim. Biophys. Acta* **1815**, 158–169 (2011).
57. Yang, Y. et al. CXCL12-CXCR4/CXCR7 Axis in Cancer: From mechanisms to clinical applications. *Int. J. Biol. Sci.* **19**, 3341–3359 (2023).
58. Tachibana, K. et al. The chemokine receptor CXCR4 is essential for vascularization of the gastrointestinal tract. *Nature* **393**, 591–594 (1998).
59. Lima e Silva, R. et al. The SDF-1/CXCR4 ligand/receptor pair is an important contributor to several types of ocular neovascularization. *FASEB J.* **21**, 3219–3230 (2007).
60. Zhang, Z. X. et al. Hypoxia specific SDF-1 expression by retinal pigment epithelium initiates bone marrow-derived cells to participate in Choroidal neovascularization in a laser-induced mouse model. *Curr. Eye Res.* **36**, 838–849 (2011).
61. Arai, Y. et al. Aqueous humour proteins and treatment outcomes of anti-VEGF therapy in neovascular age-related macular degeneration. *PloS ONE* **15**, e0229342 (2020).
62. Carmeliet, P. & Jain, R. K. Molecular mechanisms and clinical applications of angiogenesis. *Nature* **473**, 298–307 (2011).
63. Bergers, G. & Hanahan, D. Modes of resistance to anti-angiogenic therapy. *Nat. Rev. Cancer* **8**, 592–603 (2008).
64. Mitsuhashi, A. et al. Fibrocyte-like cells mediate acquired resistance to anti-angiogenic therapy with bevacizumab. *Nat. Commun.* **6**, 8792 (2015).
65. Shen, Y. et al. Reduction of liver metastasis stiffness improves response to bevacizumab in metastatic colorectal Cancer. *Cancer cell* **37**, 800–817 (2020).
66. Sakurai, A., Doci, C. L. & Gutkind, J. S. Semaphorin signaling in angiogenesis, lymphangiogenesis and cancer. *Cell Res.* **22**, 23–32 (2012).
67. Yang, W. J. et al. Semaphorin-3C signals through Neuropilin-1 and PlexinD1 receptors to inhibit pathological angiogenesis. *EMBO Mol. Med.* **7**, 1267–1284 (2015).
68. Sun, Y. et al. Sema3f protects against subretinal neovascularization in vivo. *EBioMedicine* **18**, 281–287 (2017).
69. Cerani, A. et al. Neuron-derived semaphorin 3A is an early inducer of vascular permeability in diabetic retinopathy via neuropilin-1. *Cell Metab.* **18**, 505–518 (2013).
70. Joyal, J. S. et al. Ischemic neurons prevent vascular regeneration of neural tissue by secreting semaphorin 3A. *Blood* **117**, 6024–6035 (2011).
71. Wei, Y. et al. Nrf2 in ischemic neurons promotes retinal vascular regeneration through regulation of semaphorin 6A. *Proc. Natl. Acad. Sci. USA* **112**, E6927–E6936 (2015).

72. Chen, D. Y. et al. Endothelium-derived semaphorin 3G attenuates ischemic retinopathy by coordinating beta-catenin-dependent vascular remodeling. *J. Clin. Invest.* **131**, https://doi.org/10.1172/jci135296 (2021).
73. Fukushima, Y. et al. Sema3E-PlexinD1 signaling selectively suppresses disoriented angiogenesis in ischemic retinopathy in mice. *J. Clin. Invest.* **121**, 1974–1985 (2011).
74. Wu, J. H. et al. Inhibition of Sema4D/PlexinB1 signaling alleviates vascular dysfunction in diabetic retinopathy. *EMBO Mol. Med.* **12**, e10154 (2020).
75. Dong, C. et al. Fibroblasts with high matrix metalloproteinase 2 expression regulate CD8+ T-cell residency and inflammation via CD100 in psoriasis. *Br.J. Dermatol.* **191**, 405–418 (2024).
76. Wang, L. et al. Knockout of Sema4D alleviates liver fibrosis by suppressing AOX1 expression. *Pharmacol. Res.* **195**, 106886 (2023).
77. Fisher, T. L. et al. Generation and preclinical characterization of an antibody specific for SEMA4D. *mAbs* **8**, 150–162 (2016).
78. Feigin, A. et al. Pepinemab antibody blockade of SEMA4D in early Huntington's disease: a randomized, placebo-controlled, phase 2 trial. *Nat. Med.* **28**, 2183–2193 (2022).
79. Patnaik, A. et al. Safety, pharmacokinetics, and pharmacodynamics of a humanized anti-semaphorin 4D antibody, in a first-in-human study of patients with advanced solid tumors. *Clin. Cancer Res.* **22**, 827–836 (2016).
80. LaGanke, C. et al. Safety/tolerability of the anti-semaphorin 4D Antibody VX15/2503 in a randomized phase 1 trial. *Neurol. Neuroimmunol. Neuroinflamm.* **4**, e367 (2017).
81. Shafique, M. R. et al. A phase Ib/II study of pepinemab in combination with avelumab in advanced non-small cell lung cancer. *Clin. Cancer Res.* **27**, 3630–3640 (2021).
82. Bulloj, A., Maminishkis, A., Mizui, M. & Finnemann, S. C. Semaphorin4D-PlexinB1 signaling attenuates photoreceptor outer segment phagocytosis by reducing Rac1 activity of RPE cells. *Mol. Neurobiol.* **55**, 4320–4332 (2018).
83. Li, Y. et al. A rat model for stable chronic obstructive pulmonary disease induced by cigarette smoke inhalation and repetitive bacterial infection. *Biol. Pharm. Bull.* **35**, 1752–1760 (2012).
84. Liu, S. et al. An optimized procedure to record visual evoked potential in mice. *Exp. Eye Res.* **218**, https://doi.org/10.1016/j.exer.2022.109011 (2022).
85. Cui, B. et al. Exercise alleviates neovascular age-related macular degeneration by inhibiting AIM2 inflammasome in myeloid cells. *Metab. Clin. Exp.* **144**, 155584 (2023).
86. Guo, J., Luo, X., Liang, J., Xiao, M. & Sun, X. Antiangiogenic effects of doxazosin on experimental choroidal neovascularization in mice. *J. Ocular Pharmacol. Ther.* **33**, 50–56 (2017).
87. Rho, C. R. et al. Antiangiogenic effects of topically administered multiple kinase inhibitor, motesanib (AMG 706), on experimental choroidal neovascularization in mice. *J. Ocular Pharmacol. Ther.* **31**, 25–31 (2015).
88. Love, M. I., Huber, W. & Anders, S. Moderated estimation of fold change and dispersion for RNA-seq data with DESeq2. *Genome Biol.* **15**, 550 (2014).
89. Jain, A. & Tuteja, G. TissueEnrich: Tissue-specific gene enrichment analysis. *Bioinformatics* **35**, 1966–1967 (2019).
90. Subramanian, A. et al. Gene set enrichment analysis: a knowledge-based approach for interpreting genome-wide expression profiles. *Proc. Natl. Acad. Sci. USA* **102**, 15545–15550 (2005).
91. Liberzon, A. et al. The molecular signatures database (MSigDB) hallmark gene set collection. *Cell Syst.* **1**, 417–425 (2015).
92. Liberzon, A. et al. Molecular signatures database (MSigDB) 3.0. *Bioinformatics* **27**, 1739–1740 (2011).
93. Macosko, E. Z. et al. Highly parallel genome-wide expression profiling of individual cells using nanoliter droplets. *Cell* **161**, 1202–1214 (2015).
94. Butler, A., Hoffman, P., Smibert, P., Papalexi, E. & Satija, R. Integrating single-cell transcriptomic data across different conditions, technologies, and species. *Nat. Biotechnol.* **36**, 411–420 (2018).
95. La Manno, G. et al. RNA velocity of single cells. *Nature* **560**, 494–498 (2018).
96. Jin, S. et al. Inference and analysis of cell-cell communication using CellChat. *Nat. Commun.* **12**, 1088 (2021).
97. Shen, Y. et al. STAT3-YAP/TAZ signaling in endothelial cells promotes tumor angiogenesis. *Sci. Signal* **14**, eabj8393 (2021).
98. Liu, J. et al. Heterologous prime-boost immunizations with chimpanzee adenoviral vectors elicit potent and protective immunity against SARS-CoV-2 infection. *Cell Discov.* **7**, 123 (2021).
99. Kim, S., Lee, H., Chung, M. & Jeon, N. L. Engineering of functional, perfusable 3D microvascular networks on a chip. *Lab on a Chip* **13**, 1489–1500 (2013).
100. He, H. et al. Activating NO-sGC crosstalk in the mouse vascular niche promotes vascular integrity and mitigates acute lung injury. *J. Exp. Med.* **220**, https://doi.org/10.1084/jem.20211422 (2023).
101. Lavalette, S. et al. Interleukin-1beta inhibition prevents choroidal neovascularization and does not exacerbate photoreceptor degeneration. *Am. J. Pathol.* **178**, 2416–2423 (2011).

Acknowledgements

This study was supported by the National Natural Science Foundation of China (82330031 and 82020108007 to H.Y., 82122018 and 32471169 to X.H.), the National Key R&D Program of China (2020YFA0803703 to X.H., 2021YFC2401404 to H.Y.) Natural Science Foundation of Tianjin (23JCJQJC00050 to X.W., 23JCQNJC01290 to X.D.), Tianjin Science & Technology Foundation (22PTZWHZ00030 to H.Y). We thank the Core Facility of Research Center of Basic Medical Sciences at Tianjin Medical University for technical support, we thank Dr. Zhiyan Zhu for technical support in flow cytometry.

Author contributions

X.W. and H.Y. designed the project; K.H., X.D., Z.L., Y.L., J.H., P.K., B.C., M.W. and S.Z. carried out the experiments; T.Y. and X.Y. analyzed the scRNA-seq data; W.Z. diagnosed all enrolled nvAMD patients; H.X., L.Z., J.W., Q.L. J.H., X.W. and H.Y. supervised the study and reviewed the manuscript. J.H., X.W. and H.Y. wrote the paper with the input from all authors.

Competing interests

The authors declare no competing interests.

Additional information

Supplementary information The online version contains supplementary material available at https://doi.org/10.1038/s41467-025-58074-0.

Correspondence and requests for materials should be addressed to Junhao Hu, Xiaohong Wang or Hua Yan.

Peer review information *Nature Communications* thanks Jiansheng Li, and the other anonymous reviewer(s) for their contribution to the peer review of this work. A peer review file is available.